

Outflows in Infrared-Luminous Starbursts at $z < 0.5$. I. Sample, Na I D Spectra, and Profile Fitting¹²³

David S. Rupke, Sylvain Veilleux

Department of Astronomy, University of Maryland, College Park, MD 20742

drupke@astro.umd.edu, veilleux@astro.umd.edu

and

D. B. Sanders

Institute for Astronomy, University of Hawaii, 2680 Woodlawn Drive, Honolulu, HI 96822

sanders@ifa.hawaii.edu

ABSTRACT

We have conducted a spectroscopic survey of 78 starbursting infrared-luminous galaxies at redshifts up to $z = 0.5$. We use moderate-resolution spectroscopy of the Na I D interstellar absorption feature to directly probe the neutral phase of outflowing gas in these galaxies. Over half of our sample are ultraluminous infrared galaxies that are classified as starbursts; the rest have infrared luminosities in the range $\log(L_{\text{IR}}/L_{\odot}) = 10.2 - 12.0$. The sample selection, observations, and data reduction are described here. The absorption-line spectra of each galaxy are presented. We also discuss the theory behind absorption-line fitting in the case of a partially-covered, blended absorption doublet observed at moderate-to-high resolution, a topic neglected in the literature. A detailed analysis of these data is presented in a companion paper.

¹Some of the observations reported here were obtained at the W. M. Keck Observatory, which is operated as a scientific partnership among the California Institute of Technology, the University of California, and the National Aeronautics and Space Administration. The Observatory was made possible by the generous financial support of the W. M. Keck Foundation.

²Some of the observations reported here were obtained at the MMT Observatory, a joint facility of the Smithsonian Institution and the University of Arizona.

³Some of the observations reported here were obtained at the Kitt Peak National Observatory, National Optical Astronomy Observatory, which is operated by the Association of Universities for Research in Astronomy, Inc. (AURA) under cooperative agreement with the National Science Foundation.

Subject headings: galaxies: starburst — galaxies: absorption lines — infrared: galaxies — ISM: jets and outflows — line: profiles — methods: data analysis

1. INTRODUCTION

Galaxy-scale outflows of gas, sometimes called ‘superwinds,’ have been known for some time to be a ubiquitous phenomenon in galaxies undergoing intense and spatially concentrated star formation (i.e., starburst galaxies). In these galaxies, the driving force of large-scale winds is supernova-heated gas (Chevalier & Clegg 1985). These winds are active contributors to the evolution of galaxies and the surrounding inter-galactic or intra-cluster medium (IGM/ICM) in which they are embedded. Winds have been invoked to resolve a number of issues in cosmology and galaxy evolution (e.g., Veilleux & Rupke 2004). For example, they may explain the ‘baryon deficit’ in the Galaxy (Silk 2003) and the mass-metallicity relation of galactic bulges (e.g., Bregman 1978; Kauffmann & Charlot 1998; van den Bosch 2002), resolve discrepancies between the observed and predicted galaxy luminosity functions (e.g., Somerville & Primack 1999; Cole et al. 2000), and enrich the IGM and ICM to observed levels (Renzini 1997; Buote 2000; Madau, Ferrara, & Rees 2001; Aguirre et al. 2001b; Theuns et al. 2002; Simcoe, Sargent, & Rauch 2002; though see Aguirre et al. 2005). They are often incorporated into numerical simulations of galaxy formation and evolution (e.g., Aguirre et al. 2001a; Scannapieco, Thacker, & Davis 2001; Theuns et al. 2002; Springel & Hernquist 2003), but there are not yet enough observational data to fully inform the simplified prescriptions used in the simulations. (For a recent review of the properties and implications of mechanical feedback in galaxies, see Veilleux, Cecil, & Bland-Hawthorn 2005.)

To complement and extend the current state of knowledge of superwinds, we have undertaken the largest survey to date of outflows in infrared-luminous galaxies. Our survey extends over a broad redshift range from $z = 0$ to $z = 0.5$. We have included starburst galaxies with a wide range of properties and, for the first time, searched for superwinds in a statistically significant number (43) of ultraluminous infrared galaxies (ULIRGs). ULIRGs are defined as galaxies with $L_{\text{IR}} > 10^{12} L_{\odot}$. Our pilot study of 11 ULIRGs (Rupke, Veilleux, & Sanders 2002) and a more recent study of 20 ULIRGs (Martin 2005) showed that winds occur with high frequency in these galaxies.

Ultraluminous infrared galaxies have unique properties (Sanders & Mirabel 1996). They host vigorous starbursts, but many also show significant AGN activity (Genzel et al. 1998; Veilleux et al. 1995; Veilleux, Kim, & Sanders 1999a; Veilleux, Sanders, & Kim 1999b; Lutz, Veilleux, & Genzel 1999). ULIRGs contain copious amounts of dense molecular gas in their

cores (e.g., Sanders, Scoville, & Soifer 1991; Solomon et al. 1997; Downes & Solomon 1998), which is available to power star formation. Most are late-stage mergers of two gas-rich spirals that are evolving into moderate-size elliptical galaxies (Sanders et al. 1991; Solomon et al. 1997; Genzel et al. 2001; Tacconi et al. 2002; Kim, Veilleux, & Sanders 2002; Veilleux, Kim, & Sanders 2002). Their number density increases strongly with increasing redshift, evolving approximately as $(1+z)^7$ (Kim & Sanders 1998; Chapman et al. 2003; Cowie et al. 2004). High-redshift counterparts are seen in deep submillimeter imaging, further suggesting strong density evolution (e.g., Smail, Ivison, & Blain 1997; Hughes et al. 1998; Blain et al. 1999; Lilly et al. 1999; Barger, Cowie, & Sanders 1999; Chapman et al. 2003). This redshift evolution has important implications for star formation and merger history, and is in the process of being nailed down firmly by observations with the *Spitzer Space Telescope (SST)*.

ULIRGs possess quasar-like bolometric luminosities, and are the most numerous high-luminosity objects at low redshifts. The frequency of occurrence of AGN activity in these galaxies increases with increasing infrared luminosity (Veilleux et al. 1999a) and as the merger progresses (Veilleux et al. 2002). In fact, it is hypothesized that ULIRGs play a role in the evolution of quasars. Many ULIRGs may contain buried AGN that are hidden by dust; when this dust is removed (by radiation pressure, or perhaps the outflows studied in this work), a bright quasar is left (Sanders et al. 1988). This evolutionary process is currently under scrutiny, and is probably active in some, but not all, cases (Tacconi et al. 2002; Veilleux et al. 2002).

Luminous infrared galaxies (LIRGs; $10^{11} < L_{\text{IR}}/L_{\odot} < 10^{12}$) host less intense starbursts than ULIRGs. They fall into two groups (Ishida 2004). Half are early in the merger sequence of two roughly equal-mass galaxies, and are thus the progenitors of ULIRGs (Arribas et al. 2004; Ishida 2004). Other LIRGs are less-massive mergers or isolated disk galaxies which may or may not be experiencing an interaction (Ishida 2004). In our work, we combine LIRGs and some less-luminous galaxies ($L_{\text{IR}}/L_{\odot} < 10^{11}$) into a single group, which we label IRGs (for InfraRed Galaxies).

The ULIRGs and IRGs we have selected probe the medium-to-high star formation rate end of the starburst phenomenon. Coupled with studies of outflows in dwarf starbursts (e.g., Schwartz & Martin 2004), we can learn about the starburst phenomenon over a wide range of galaxy properties. Furthermore, these infrared-luminous galaxies are important sites of obscured star formation at redshifts above unity, as seen in sub-mm galaxy counts (see references above). Early results from *SST* indicate that ULIRGs may contain half of the forming stars at $z = 2$ (Perez-Gonzalez et al. 2005). By studying outflows in these galaxies at low redshift, we can learn how they have impacted galaxy evolution and the IGM in previous epochs.

The 78-galaxy sample we discuss in this paper consists of 35 IRGs, 30 low-redshift ULIRGs, and 13 ULIRGs with redshifts in the range $0.25 < z < 0.5$. We observed these galaxies in the Na I D doublet absorption feature ($\lambda\lambda 5890, 5896$) at moderately high spectral resolution ($65 - 85 \text{ km s}^{-1}$). Because of the low ionization potential of ground-state Na (5.14 eV), this doublet feature probes neutral gas. It is not redshifted out of the visible until $z \sim 0.5$, making it a useful indicator over a wide range of cosmic times. Furthermore, in the young starbursts that are found in most of our objects, Na atoms are ionized in hot stars and the stellar Na I D line is relatively weak; the interstellar Na I abundance remains high, however. Finally, its doublet nature resolves a degeneracy in optical depth and covering fraction. Blueshifted velocity components in this feature unambiguously indicate the presence of outflowing gas, as demonstrated in previous studies (Phillips 1993; Heckman et al. 2000; Rupke et al. 2002; Schwartz & Martin 2004; Martin 2005).

We have taken special care with the Na I D profile fitting in this work and discuss our methods in detail. This care is motivated by (a) the fact that simple Gaussian fitting is not appropriate for mildly saturated features, which we observe in many cases; (b) the need to decompose the broad, blended doublet lines we observe in many spectra; and (c) the need to deal with non-zero covering fraction in most spectra. These issues have been partially addressed in the past but it is useful to discuss them here in the light of the advent of high-resolution spectrographs for deep galaxy surveys.

This paper describes the sample selection, observations, and data reduction for our survey, in §§2–3. The absorption-line spectra of each galaxy are presented in §4. We discuss the theory behind absorption-line fitting in the case of a partially-covered, blended absorption doublet in §5. In §6 we discuss the actual profile fitting. §7 deals with the computation of Na and H column densities. In the Appendix, we note unusual properties of individual galaxies. A detailed analysis of these data is presented in a companion paper (Rupke, Veilleux, & Sanders 2005a, hereafter Paper II).

For all calculations, we assume present-day values for the cosmological parameters of $H_0 = 75 \text{ km s}^{-1} \text{ Mpc}^{-1}$ and the standard $\Omega_m = 0.3, \Omega_\Lambda = 0.7$ cosmology. All wavelengths quoted are vacuum wavelengths (except those used as labels for spectral lines) and are generally taken from the NIST Atomic Spectra Database¹. (One exception is the vacuum wavelengths of Na I D, which are 5891.58 and 5897.55 Å; Morton 1991.)

¹http://physics.nist.gov/cgi-bin/AtData/main_asd

2. SAMPLE

For this study we have selected infrared-bright galaxies whose infrared luminosities are dominated by dust-reprocessed radiation from a starburst. To avoid contamination from a strong AGN, we have chosen galaxies with nuclear optical spectral types of LINER or H II-region-like. This choice favors starburst-powered luminosities, as suggested by mid-infrared diagnostics of ULIRGs (Genzel et al. 1998) and the good correspondence of optical and mid-infrared spectral classifications (Lutz et al. 1999). However, some LINERs may contain buried (but not energetically dominant) AGN; for instance, VLA observations show compact radio cores in a number of ULIRG LINERs (Nagar et al. 2003).

We have also deliberately selected galaxies with a wide range of infrared luminosities ($L_{\text{IR}} \equiv L[8-1000 \mu\text{m}]$) and redshifts in order to probe the dependence of outflow properties on galaxy properties. Our final sample consists of 78 starburst-dominated galaxies. We subdivide the sample by L_{IR} and redshift. Figure 1 shows the distribution of star formation rate and redshift in our three subsamples. Tables 1 and 2 list the average properties of each subsample and the individual properties of each galaxy, respectively.

Star formation rate (SFR) follows directly from L_{IR} according to (Kennicutt 1998)

$$\text{SFR} = \alpha \frac{L_{\text{IR}}}{5.8 \times 10^9 L_{\odot}}. \quad (1)$$

We have modified this equation by the coefficient α , which is the fraction of L_{IR} powered by star formation. Results from the *Infrared Space Observatory (ISO)* suggest that 70% – 95% of the infrared luminosity of a typical ULIRG is powered by star formation (Genzel et al. 1998). Thus, we assume $\alpha = 0.8$ for all of our ULIRGs. However, we assume $\alpha = 1.0$ for the IRGs.

2.1. $z < 0.25$ ULIRGs

Most of these galaxies are taken from the 1 Jy survey (Kim & Sanders 1998). The 1 Jy survey is a complete sample, down to a flux level of $f_{\nu}(60 \mu\text{m}) = 1 \text{ Jy}$, of 118 ULIRGs observed by the *Infrared Astronomical Satellite (IRAS)* with Galactic latitude $|b| > 30^\circ$ and declination $\delta > -40^\circ$. These objects have redshifts of $z = 0.02 - 0.27$ and are the brightest sources with luminosities in the range $\log(L_{\text{IR}}/L_{\odot}) = 12.01 - 12.84$. We have slightly increased the published infrared luminosities to correspond to the standard cosmology.

We also include three nearby ULIRGs that are not part of the 1 Jy survey: F10565+2448, F17207–0014, and *IRAS* 20046–0623. The latter two are excluded from the 1 Jy sample

due to their low Galactic latitude, while the first is excluded because its luminosity is slightly lower using older fluxes. A single object from the FIRST/FSC survey (Stanford et al. 2000) is also part of the low- z subsample.

We selected the brightest galaxies which have H II or LINER optical spectral classifications based on low-dispersion spectroscopy (Kim, Veilleux, & Sanders 1998; Veilleux et al. 1999a). Six of the galaxies in this subsample were observed in the mid-infrared with *ISO* and are classified as starbursts; one other (F17068+4027) has an AGN classification (Lutz et al. 1999). Ten galaxies (including F17068+4027) were observed in the near-infrared and show no evidence of broad-line regions.

2.2. $0.25 < z < 0.5$ ULIRGs

These galaxies were selected from the FIRST/FSC survey (Stanford et al. 2000). The FIRST/FSC survey is a cross-correlation of faint $60\ \mu\text{m}$ and $100\ \mu\text{m}$ point sources from the *IRAS* Faint Source Catalog (FSC) with 1.4 GHz point sources in the VLA FIRST database. This technique yields distant infrared-luminous galaxies because of the tight radio/far-infrared flux relationship for galaxies (Condon, Anderson, & Helou 1991). The resulting sample consists of 108 sources with $\langle z \rangle = 0.31$. We selected targets from the FIRST/FSC catalog that have appropriate L_{IR} and z , are not highly nucleated and do not have high very high radio fluxes (to avoid selecting Seyfert 1 galaxies), and have the brightest K -band fluxes (for observability).

Since in most cases the 12 and $25\ \mu\text{m}$ fluxes of these galaxies are too faint to be measured by *IRAS*, L_{IR} cannot be calculated using the usual formula (though the contribution of the 12 and $25\ \mu\text{m}$ fluxes to L_{IR} is small; Sanders & Mirabel 1996). For many of these sources, infrared luminosities were calculated by including radio fluxes in the SED fitting and using the radio/infrared correlation (Blain, Barnard, & Chapman 2003; Andrew Blain, private communication). Where these luminosities are not available, we have used the observed 60 and $100\ \mu\text{m}$ fluxes and scaled them to get the 12 and $25\ \mu\text{m}$ fluxes (Kim & Sanders 1998) to compute the infrared luminosity. The difference between these two methods is generally small when both are possible.

One object from the 1 Jy survey (Kim & Sanders 1998), F04313–1649, also falls in this subsample.

2.3. IRGs

To study trends in outflow properties over a large range of SFR, we observed infrared-selected galaxies with infrared luminosities in the range $\log(L_{\text{IR}}/L_{\odot}) = 10.2 - 12.0$ (median 11.36). Hereafter we refer to these galaxies as IRGs, rather than LIRGs, since some have $\log(L_{\text{IR}}/L_{\odot}) \leq 11.0$. The bulk of our galaxies were culled from the *IRAS* Revised Bright Galaxy Sample (RBGS; Sanders et al. 2003) and the Warm Galaxy Survey (WGS; Kim et al. 1995). We chose objects with measured optical spectral types (of H II or LINER). We also selected relatively distant objects ($\langle z \rangle = 0.032$) to minimize aperture- and distance-related effects when comparing the three subsamples. The morphologies of these galaxies, as determined from DSS2 and 2MASS images, are varied; some are relatively normal disks, while others are obviously undergoing an interaction with another galaxy.

Two of the galaxies in this subsample, F09320+6134 (UGC 5101) and F16504+0228 (NGC 6240), were observed in the mid-infrared with *ISO* and are classified as starbursts (Lutz et al. 1999). We also observed one object at $z = 0.479$ from a 12 μm *ISO* survey (Clements et al. 1999; Clements, Desert, & Franceschini 2001). The infrared luminosity for this object, F1.5, is extrapolated from the 12 μm luminosity assuming a starburst SED and is thus uncertain.

2.4. Other Properties

In Table 2, we list the K - or K' - and R -band absolute magnitudes of each galaxy. The difference between the transmissions of the K and K' filters is minimal (~ 0.05 mag; Wainscoat & Cowie 1992), so we use these interchangeably. For the 1 Jy galaxies, these are host galaxy magnitudes (Veilleux et al. 2002). For the FIRST/FSC galaxies, we have only total K -band magnitudes (Stanford et al. 2000). For the rest of our sample, total K_s magnitudes are taken from the 2MASS Large Galaxy Atlas where available (Jarrett et al. 2003); otherwise, we use 2MASS K magnitudes down to an isophote of 20 mag/ \square'' . Optical magnitudes for the non-1 Jy galaxies are from Armus, Heckman, & Miley (1990) or Lehnert & Heckman (1995).

This table also lists the measured circular velocity v_c for each galaxy. We assume $v_c^2 = 2\sigma^2 + v_{\text{rot}}^2$. For many of the ULIRGs, we have measurements of stellar velocity dispersions and rotational velocities (Genzel et al. 2001; Tacconi et al. 2002; K. Dasyra, private communication). In ULIRGs, the velocity dispersion typically dominates v_c ; for the few galaxies without measured stellar rotational velocities, we use the median value relative to σ in ULIRGs, $v_{\text{rot}}/2\sigma = 0.42$ (K. Dasyra, private communication).

For the IRGs, most of our measurements are of the gas rotational velocities. These come from inclination-corrected optical ($H\alpha$) measurements from our data or other sources (Lehnert & Heckman 1995; Heckman et al. 2000; Murphy et al. 2001) or are based on H I linewidths (Mirabel & Sanders 1988; Hutchings 1989; Martin et al. 1991; van Driel, Gao, & Monnier-Ragaine 2001) using the formulas of Lehnert & Heckman (1995).

Most of the objects in our sample are single-nucleus galaxies. However, given that ULIRGs are in the late stages of equal-mass mergers (Veilleux et al. 2002), we would expect multiple nuclei in some of these galaxies. In fact, there are 10 objects in our sample which have well-resolved double nuclei, 8 of which are ULIRGs. In each case we have taken spectra of both nuclei. However, there are certainly multiple nuclei with very small separation (not resolved in our spectra) in other galaxies in our sample, such as the well-known case F16504+0228 (NGC 6240).

In Appendix A, we list unusual properties of a handful of individual galaxies.

3. OBSERVATIONS AND DATA REDUCTION

3.1. Observations

The data were taken over the course of 14 observing runs at three different facilities. These observing runs are listed in Table 3. Most observations were made in photometric conditions. We achieved a median signal-to-noise ratio near Na I D of 26 per \AA and a range of 10 – 100 per \AA .

For the most distant targets, we used the Echellette Spectrograph and Imager (ESI; Sheinis et al. 2002) on Keck II in echellette mode. With a $1''.0$ slit width, we obtained a constant spectral resolution of $R \sim 4600$, or 65 km s^{-1} FWHM, over the wavelength range $4000\text{--}11000 \text{ \AA}$. For some of our median-redshift data, we used the Red Channel Spectrograph on the MMT, with an echellette grating. We used two different setups, one including orders 6 – 13 ($4500\text{--}10200 \text{ \AA}$), the other using orders 7 – 13 ($4300\text{--}8800 \text{ \AA}$). With a $1''.0$ slit, we obtained a spectral resolution that varies from order to order but averages $R \sim 3400$, or 87 km s^{-1} .

For the nearest targets, we used the R-C Spectrograph on the Kitt Peak 4m. We used the KPC-18C grating in 1st order, which is a compromise between high resolution and good wavelength coverage, and the T2KB detector. The slit width was $1''.0\text{--}1''.5$, yielding an average spectral resolution at 6300 \AA of $R \sim 3500$, or 85 km s^{-1} , with a variation of $10\text{--}15 \text{ km s}^{-1}$ around this value. We observed 1700 \AA in one exposure, allowing us to

measure Na I D and the $H\alpha/[N II]$ complex at once.

The slit position angles listed in Table 2 were generally chosen to be randomly oriented with respect to the galaxy, either at 0° or near the parallactic angle. For most double-nucleus galaxies, however, we deliberately positioned the slit to connect the two nuclei in a single observation.

3.2. Data Reduction

Standard data processing techniques were used to reduce our data. For the long-slit and MMT data, we used IRAF routines for the basic reductions. For the ESI data, we used MAKEE², which is a publicly-available data reduction pipeline. In each case, Poisson error spectra were propagated in parallel with the data, since these errors are necessary for profile fitting (§6). Our output wavelengths are vacuum heliocentric.

The long slit data were not flatfielded, in order to retain the statistical weights of the raw data. However, fringing is not a problem for these data. The MMT and ESI data were flatfielded to remove fringing and other defects, which are severe in the reddest orders. The spectral extraction of the echellette data was performed using ‘optimal’ extraction techniques (Horne 1986; Marsh 1989). This extraction takes care of defects and cosmic rays; for the long slit data, we removed cosmic rays by hand in the regions of interest.

HeNeAr lamps were used to wavelength-calibrate the long slit and MMT data; CuAr, HgNe, and Xe lamps were used simultaneously for the ESI data. A number of standard stars were used for flux calibration; the most effective ones are those with smooth continua free of metal absorption lines, such as G191-B2B and Feige 34 (which are both hot dwarfs). Because the ESI data is finely sampled and of moderately high resolution, the flux standards we chose have closely-spaced wavelength points, and any absorption features were carefully avoided.

We generally extracted as much of the galaxy continuum light as possible. In some cases faint continuum or emission-line spatial extensions are present in the spectra, especially in the nearest galaxies, but we did not extract these regions if it seriously harmed the signal-to-noise of the extracted spectra. The result is that the linear size probed in each galaxy is different (though not dramatically so), depending on the light distribution and redshift of the galaxy. It would have been desirable to extract a constant linear aperture for each galaxy, both for determining the properties of potential outflows and for computing nuclear

²<http://www2.keck.hawaii.edu/inst/common/makeewww/index.html>

spectral types of galaxies. Practically, this was not possible due to the large redshift range in our sample.

Before fitting the Na I D feature, we divided the continuum by a Legendre polynomial fit (of order 2 – 6) using 100 Å of data on either side of the He I λ 5876 – Na I D complex.

3.3. Spectral Types

Each galaxy is classified as an H II galaxy or a LINER. For those objects for which nuclear optical spectral types are not available from previous data (mostly galaxies from our high- z subsample), we determined them using the line ratio diagrams of Veilleux & Osterbrock (1987). There are four galaxies for which the spectral type is ambiguous because either H α or [O III] λ 5007 are unobserved or absorbed by resonance lines in the atmosphere, but there is sufficient evidence in each case to effectively rule out a dominant AGN (see Appendix A).

The primary uncertainty in our spectral type measurements is increasing aperture size with redshift. The aperture is rectangular, with one side being the slit width ($\sim 1''$) and the other the extraction size along the slit. A $1''$ slit width projects to 5 kpc at $z \sim 0.4$. The extraction region along the slit is even larger. Thus, starburst light from the host galaxy (of spectral type H II) could dilute the light from an AGN (of spectral type Seyfert), especially weak broad-line regions. For this reason, the spectral types in our high- z subsample should be considered somewhat uncertain.

3.4. Redshifts

For each galaxy, we take the redshift from the following sources, in order of preference: (1) nebular emission-line rotation curves (our data); (2) H I emission or absorption lines (Mirabel & Sanders 1988; Hutchings 1989; Martin et al. 1991; van Driel et al. 2001); (3) stellar absorption line centroids (our data); or (4) nebular emission line centroids (our data). H I data is available for ~ 20 of the nearest galaxies in our sample. In those cases where they agree, we use the H I velocity instead of the rotation curve centroid, since the former is more precise. Stellar absorption lines are preferable to nebular emission lines for finding the systemic velocity of the galaxy. However, in many cases we do not observe these lines or their S/N is too low, and we must resort to using emission lines. In both cases we average over as many strong lines as possible.

In many galaxies (mostly IRGs), the optical emission lines indicate rotation. For these

galaxies, the redshift is the average of the velocities of the emission-line lobes of the rotation curve. Other emission-line profiles show a single lobe, in which the sizes of the core and wings of the profiles vary greatly. The ULIRGs tend to show complex and broad profiles. In asymmetric profiles where there is no obvious rotation and the profile is too irregular to fit with an analytic function, we have generally used the redshift of the peak of the line. To de-blend adjacent emission lines (e.g., $H\alpha/[N\ II]$ or $[S\ II]\ \lambda\lambda 6716, 6731$), we fit analytic profiles to the lines, which generally yields a flux-averaged redshift.

The uncertainties in our redshift determinations (both measurement and systemic) are ± 0.00005 on average, or $15\ \text{km s}^{-1}$. The 1σ measurement uncertainties in the outflow velocity of the neutral gas are comparable ($\sim 10\ \text{km s}^{-1}$ on average; see Table 4). Wavelength calibration uncertainties are generally smaller, but comparable, at $\lesssim 10\ \text{km s}^{-1}$. However, the systematic uncertainties in these quantities are unknown.

4. SPECTRA

Figures 2 – 4 display the spectra and line fits for our three subsamples. The data are binned in $\sim 35\ \text{km s}^{-1}$ bins for the echellette data and slightly larger bins ($50 - 60\ \text{km s}^{-1}$) for the KPNO data, in each case using variance weighting. The horizontal axes show the velocity relative to systemic of the $\text{Na I D}_2\ \lambda 5890$ line. These spectra are analyzed and discussed in detail in Paper II.

5. PHYSICAL INTERPRETATION OF BLENDED ABSORPTION DOUBLETS

Absorption line profiles can be classified in a number of ways that affect the choice of analysis technique:

- **Instrumental Resolution.** Is the line resolved or unresolved by the spectrograph?
- **Number of transitions.** How many transitions of a given atomic or molecular state are available? If there are multiple transitions, are they blended or unblended?
- **Optical depth and covering fraction.** Is the line optically thin or optically thick? Is the covering fraction of the absorbing gas less than unity?
- **Velocity distribution.** Can the velocity distribution be described by a simple function like a Gaussian (i.e., the ‘curve-of-growth’ assumption)? Can it be described by

overlapping components of a simple function?

In this section, we will first briefly review the effect of a covering fraction that is not unity on absorption line fitting. Our particular focus, however, will be the impact of blending of two or more lines of a multiplet on fitting. Our data is typically well-resolved, but the lines of the Na I D doublet are blended because of the intrinsic broadening of the absorbing gas. The issue of blending is neglected in the literature.

5.1. Covering Fraction

For a single line, the distribution of optical depth along the line-of-sight can be computed exactly as a function of velocity if the covering fraction of the gas is unity (in other words, if the absorbing gas completely covers the background source). This is generally the case for quasar or stellar sight lines through the intergalactic and interstellar media, respectively, since the background light source in each of these cases is a point source. This analysis can also be done for blended doublet, triplet, or multiplet lines by solving a set of linear equations, Gaussian fitting, or ‘regularization’ methods (Arav et al. 1999b).

In the case where the background light source subtends a large angle on the sky relative to the absorbing gas, the covering fraction is not in general unity. Examples include a galaxy starburst that illuminates gas clouds in the halo of the galaxy, or clouds in the broad-line region near a quasar. In these cases, a degeneracy arises when solving for optical depth and covering fraction for a single line. This degeneracy is typically broken by observing two or more transitions in the same ion, with the same lower level, whose relative optical depths can be computed exactly from atomic physics.

5.2. Multiple Unblended Transitions

Multiple transitions are necessary for constraining the optical depth of a line when the covering fraction is less than unity. Whether or not these lines are blended or not depends on their separation and on the astrophysical context (are the lines intrinsically broad or narrow?). An example of resolved, unblended lines are the broad, interstellar Ca II H & K lines seen in Mrk 231 (Rupke et al. 2002); these lines have widths of several hundred km s^{-1} , but the H & K lines are separated by several thousand km s^{-1} . In the same galaxy, we observe Na I D lines with widths of $\gtrsim 1000 \text{ km s}^{-1}$; the two lines of the doublet are, however, separated by only 300 km s^{-1} . The Na I D lines in this galaxy are thus resolved and blended.

For the case of multiple resolved, unblended lines in the same ion that arise from the same energy level, it is trivial to calculate both optical depth and covering fraction as a function of velocity. No velocity distribution must be assumed. The intensity in a line is a unique function of optical depth and covering fraction at each velocity. The optical depths of the different lines in a multiplet are related by atomic physics, and their covering fractions are the same, such that one can solve a set of simple equations to get τ and C_f as a function of velocity. The only caveat is that the optical depth ratio of at least two of the lines in the multiplet should be substantially different from unity.

These techniques are discussed in a number of papers on intrinsic quasar absorption lines in the UV (e.g., Barlow & Sargent 1997; Hamann et al. 1997; Arav et al. 1999a,b). Note that the optical depths and covering fractions determined this way are still subject to uncertainties, since they are averages along the line-of-sight and across the continuum source. Furthermore, the covering fraction determined in this way also includes light scattered into the line of sight. (Other subtleties of interpretation exist, but are beyond the scope of this discussion.)

The classic alternative to this for two unresolved (but still unblended lines) is the doublet ratio method (Nachmann & Hobbs 1973). The equivalent width for a single line is given by

$$W_{eq} = \int_0^\infty [1 - I(\lambda)] d\lambda. \quad (2)$$

For a partial covering fraction and optical depth that depend on velocity, the general expression for the intensity of an absorption line, assuming a continuum level of unity, is

$$I(\lambda) = 1 - C_f(\lambda) + C_f(\lambda)e^{-\tau(\lambda)}. \quad (3)$$

Under the curve-of-growth (COG) assumption (i.e., a Maxwellian velocity distribution), the optical depth τ can be expressed as a Gaussian:

$$\tau(\lambda) = \tau_0 e^{-(\lambda - \lambda_0)^2 / (\lambda_0 b / c)^2}, \quad (4)$$

where τ_0 and λ_0 are the central optical depth and central wavelength in the line and b is the width of the line (specifically, the Doppler parameter $b = \sqrt{2}\sigma = \text{FWHM}/[2\sqrt{\ln 2}]$).

The doublet ratio method uses the ratio of the equivalent widths of the two lines of a doublet, $R \equiv W_{eq,2}/W_{eq,1}$. R is independent of covering fraction as long as C_f is independent of velocity, since C_f appears under the integral for W_{eq} in equation (2). Assuming a constant C_f and a Maxwellian velocity distribution, the equivalent width ratio R is a monotonic

function of the central optical depth of either line (see equation [2-39] and Table 2.1 in Spitzer 1968). We can thus determine the central optical depth from the measured equivalent widths and compute the total gas column density (from equations [2-40] or [2-41] in Spitzer 1968). With knowledge of the optical depth, the covering fraction then follows from the residual intensity of the doublet lines.

If the actual velocity distribution is not Maxwellian, the doublet ratio method can underestimate the true optical depth. Nachmann & Hobbs (1973) explore the case of a 2-component profile (i.e., two overlapping Gaussian profiles in a single transition). They show that narrow, saturated components can carry a small fraction of the actual line-of-sight mass but dominate the equivalent width of the line and cause an underestimate of τ .

There are generic cases in which a superposition of components can accurately mimic the behavior of a Maxwellian, however (Jenkins 1986). A few superposed components do not, as discussed above. But a combination of many components, even if a few are mildly saturated (with optical depths $\tau \sim 5 - 10$), can produce good results under the doublet ratio method (i.e., the ratio of computed to actual column densities $N_{computed}/N_{actual} \sim 0.8 - 1.0$; Jenkins 1986). This result holds whether or not the components actually overlap in velocity space. However, it does assume that the individual components are approximately Maxwellian and that the distributions of their parameters (Doppler parameter b and optical depth τ) are not too strange (Jenkins 1986).

5.3. Multiple Blended Transitions

The case where lines in a doublet or other multiplet are blended together applies to our data, and is thus of particular interest. In the following discussion, we limit ourselves to a doublet, for simplicity and because it is relevant to this work.

We cannot simply integrate the spectrum to get the equivalent widths of the doublet lines, since they are blended. Nor can we solve for τ and C_f directly, since in the region of overlap the solution is not unique. We must thus fit analytic profiles to the lines.

One method of solution is to fit simple functional forms (such as Gaussian or Voigt profiles) to the intensity as a function of wavelength, measure the resulting equivalent widths, and use the doublet ratio to determine the optical depth of the line. Recall that the doublet ratio method assumes a Maxwellian velocity distribution and a covering fraction that is independent of velocity.

A Maxwellian velocity distribution (equivalent to a Gaussian in optical depth) only

translates into a Gaussian in intensity in the case of optically thin gas. If fitting Gaussian intensity profiles leads to a high optical depth ($\tau \gtrsim 1$) in either line, one of the assumptions of the doublet ratio method is incorrect. One result of this failure of the method is that different formulas (e.g., equations [2-40] and [2-41] in Spitzer 1968) give different values for the column density!

The doublet ratio method can give approximately correct results if there is a superposition of many components (Jenkins 1986). As we discuss above, this is true even if the intensity profile is Gaussian and some of the components are mildly saturated ($\tau \sim 5 - 10$). The profile shape may also be governed by the covering fraction rather than the optical depth, in which case optically thick gas could produce a Gaussian in intensity. Since in this case the covering fraction is not constant, the assumptions of the doublet ratio method do not apply; this method instead overestimates the true optical depth, as we show in Figure 5 (see also Arav et al. 1999a, 2003).

A second method of solution is to allow more complex intensity profiles, which are direct functions of physical parameters (e.g., velocity, optical depth, and covering fraction). The obvious benefit of this is that the profile shape is readily understood in terms of these physical parameters and the chosen optical depth and covering fraction distributions. Furthermore, different assumptions about these distributions can be tried. This method is preferable to the first in the case of a Maxwellian velocity distribution and constant C_f , since it accurately treats the intensity profile at both low and high optical depth. It has the same drawback of the first method of requiring *some* assumption about the form of these, but it is at least explicit about these assumptions.

The Na I D lines are generally blended together in our data into a single feature, and some have a covering fraction less than unity. We choose to use the second method of analysis described above. For simplicity, we assume a Maxwellian velocity distribution. In the current analysis we have restricted ourselves to a constant covering fraction, for simplicity. However, exploring non-constant C_f using analytic profiles would be interesting and useful.

5.4. Multiplet Blending and Geometry

Decomposing blended profiles correctly also requires assumptions about the geometry of the absorbing gas. The relationship between the intensity profile and the physical parameters depends not only on the optical depth and covering fraction distributions, but also on the geometry. Consider the following three cases, discussed in the context of the Na I D doublet as a specific example. We show schematics of these absorber geometries in Figure

6. Note that at a given wavelength, the atoms producing the D₁ line are separated by 6 Å ($\sim 300 \text{ km s}^{-1}$) from the atoms producing the D₂ line. However, at a given velocity relative to systemic, we expect them to have (a) relative optical depths determined by atomic physics and (b) the same covering fraction. The components described below may either be the members of a doublet or two separate velocity components of the same transition.

1. **Completely overlapping atoms.** Suppose that the atoms at all velocities are located at the same position in the plane of the sky relative to the background continuum source. This is unlikely to be strictly true if the broad profiles we observe are due to the large-scale motions of individual clouds, as these clouds are not all coincident, but it may be a good simplification. The covering fraction in this case is independent of velocity. The correct expression for the combined intensity of two separate velocity components (each with optical depth $\tau_i(\lambda)$ and covering fraction $C_{f,i}(\lambda) = C_f$) is then given by

$$I(\lambda) = 1 - C_f + C_f e^{-\tau_1(\lambda) - \tau_2(\lambda)}. \quad (5)$$

2. **Non-overlapping atoms.** Suppose that at a specific wavelength, the atoms producing the absorption have no spatial overlap in the plane of the sky. The covering fraction may be constant or velocity-dependent. The total intensity is given by

$$I(\lambda) = 1 - C_{f,1}(\lambda) - C_{f,2}(\lambda) + C_{f,1}(\lambda)e^{-\tau_1(\lambda)} + C_{f,2}(\lambda)e^{-\tau_2(\lambda)} = I_1(\lambda) + I_2(\lambda) - 1, \quad (6)$$

where I_i is the total intensity for a single absorbing component, as given in equation (3). In this case, the total covering fraction at any wavelength is subject to the constraint

$$C_{f,total} = C_{f,1} + C_{f,2} \leq 1. \quad (7)$$

3. **Partially overlapping atoms.** A ‘middle-ground’ assumption is that there is overlap at a given wavelength between the atoms producing the components, and that the covering fraction describes the fractional coverage of both the continuum source and also of the atoms producing the other component. The correct expression for the intensity is then

$$I(\lambda) = [1 - C_{f,1}(\lambda) + C_{f,1}(\lambda)e^{-\tau_1(\lambda)}] \times [1 - C_{f,2}(\lambda) + C_{f,2}(\lambda)e^{-\tau_2(\lambda)}] = I_1(\lambda)I_2(\lambda). \quad (8)$$

This formulation also allows for either a constant covering fraction or one that varies with velocity. It contains the expression for our second case plus a cross term involving

the product $C_{f,1}C_{f,2}$. In this case, the total covering fraction of the continuum source at a given wavelength is

$$C_{f,total} = C_{f,1} + C_{f,2} - C_{f,1}C_{f,2}. \quad (9)$$

In our analysis, we use a mixture of the above cases. To combine the intensities of the two doublet lines within a given velocity component, we assume the case of complete overlap and use equation (5). In reality there may be spatial variation within a given component, especially when we consider that at a given wavelength the velocity separation between the doublet lines is 300 km s^{-1} . However, we use the simplest assumption here.

To combine two different velocity components, we assume partial overlap and use equation (8). Case 1 is unlikely, since different components should have different covering fractions if we assume they are spatially distinct. Case 2 is possible, but we still consider case 3 the most likely.

6. LINE FITTING

In this section, we briefly discuss the numerical techniques used to fit our data. The results of our fitting for each galaxy are listed in Table 4. We list here for each velocity component the following: the observed wavelength of the Na I D₁ line; the velocity relative to systemic; the Doppler width; the central optical depth of the Na I D₁ line; the covering fraction; the Na I column density; and the hydrogen column density. The formulas necessary to compute $W_{eq}(\text{Na I D})$ are discussed in §5, and the equations for $N(\text{Na I})$ and $N(\text{H})$ are found in §7.

6.1. Method

To fit each Na I D feature, we use a Levenberg-Marquardt (L-M) fitting routine from Numerical Recipes (Press et al. 1992), modified to include bound constraints. These constraints are generally obvious and straightforward (e.g., $0 < C_f < 1$), and are most important in bounding the optical depth, as we discuss below. Our code, LMFIT, is written in the C programming language.

Because the L-M algorithm is a local optimizer, the number of components we choose and the initial parameter values are of some importance. We generally fit 1 – 3 velocity components, as this seems to be the maximum number that is well-constrained by our data.

Adding more components has a tendency to create components with either very high or very low optical depths. We determine by eye the initial parameter values for input to the fitting routine. The final solution (i.e., set of parameters) is in general not strongly sensitive to these initial guesses. However, in the instances that it is, the tendency is for the solution to approach high optical depths ($\tau \gg 1$). This shows up either as the parameter moving to the boundary of acceptable parameters or as long tails in the simulated optical depth distributions (§6.3) in cases where the best-fit optical depth is only a few. For most of these cases we set the optical depth as a lower limit to the true value. The most important boundary constraint is thus the optical depth upper limit, which we generally set to be ~ 5 (as the fitting is insensitive to changes in optical depth above this value because of the minimal change in the profile shape). Fortunately, the number of components with lower limits on τ is small (only 13% of components). These components are marked in Table 4.

To fit the He I $\lambda 5876$ line (15 Å blueward of Na I D), we use 1–2 Gaussian components. If the profile is not a single Gaussian, we model it on the basis of other emission lines. We usually constrain its wavelength or the wavelengths of its components to match those of other emission lines.

Ideally, LMFIT should convolve the expected profile shape with the instrumental resolution, prior to the actual fitting. This convolution adds computation time, which becomes important when simulating parameter errors. Furthermore, the instrumental response function for our data is not always Gaussian, especially for the data with slit widths comparable to or larger than the intrinsic spectral resolution (e.g., our high-resolution Keck data). For these set-ups, the intrinsic profile tends to be flat-topped. Accurately measuring this profile should be possible with a sufficient number of sky lines. Numerical simulations show that instrumental smearing has no significant impact on our data, however, and we ignore it.

6.2. Comparison to SPECFIT

The interactive fitting package SPECFIT³ is commonly used in optical spectroscopy, since it is bundled with IRAF and has a range of analytic functions that can be fit to the data (Kriss 1994). SPECFIT includes an L-M optimizer, along with several other minimization options. In Rupke et al. (2002), we used SPECFIT and added an analytic function for an absorbing doublet with a Gaussian in optical depth and a partial (but constant) covering fraction.

³<http://www.pha.jhu.edu/~gak/specfit.html>

We compared our finished code, LMFIT, to the SPECFIT L-M optimizer, since the latter is a frequently used and already tested code. We find that LMFIT converges much more quickly, but the resulting parameters are similar to those obtained with SPECFIT. However, on close inspection we discovered some minor problems with SPECFIT, primarily in how it treats parameter boundaries. (1) If the solution is across a parameter boundary after a predetermined number of iterations, SPECFIT automatically fixes the value of this parameter at the boundary and stops varying it. This can artificially constrain the parameter before the minimum is reached. (2) The L-M algorithm enforces the parameter limits after each iteration (which in parameter phase space corresponds to moving the solution back to the boundary in one dimension) at the wrong time, such that the computed χ^2 applies to the position across the boundary, not the corrected position. (3) The L-M algorithm in SPECFIT makes a stepwise numerical approximation to the first derivative using central differences; while some approximation to the second derivative matrix should be made to avoid singularities, the exact first derivative is easy to compute from the model function and not computationally expensive.

6.3. Parameter Errors

6.3.1. Monte Carlo Simulations

To determine errors in the fitted parameters, we used Monte Carlo simulations. To do this, we first assumed the fitted parameters represent the ‘real’ parameter values. We then added random Poisson noise to a ‘real’ spectrum, where the magnitude of the errors was estimated from the data. We repeated this 1000 times, each time fitting the resulting spectrum. This yielded a distribution of fitted parameters for each galaxy. The distributions in wavelength, λ , and Doppler parameter, b , are generally Gaussian, which is consistent with the assumptions of finding a best fit by minimizing χ^2 . Fits to these Gaussians yield 1σ errors in each parameter.

This method was chosen as an alternative to estimating errors directly from the covariance matrix that is output by the fitting algorithm or from two-dimensional χ^2 contours. Given the large number of parameters involved, some of which are not completely independent of each other, it would be uninformative to simply quote these errors.

The covariance matrix output from our fitting routine shows that in general the covering fraction and optical depth are anti-correlated within a given velocity component. Because of this, we examined the distribution of the product $C_f \times \tau$, rather than of C_f or τ separately. In the case of high S/N data, $C_f\tau$ is typically distributed as a Gaussian. However, for most

components, this product has a tail to high values, of varying length. Instead of fitting a Gaussian to the distribution in $C_f\tau$, we compute 68%-confidence errors both above and below the mean. When propagating these errors to other quantities, we typically assume that the percent error is split evenly between C_f and τ . However, if τ is a lower limit, we set the upper error in C_f to equal the lower error.

6.3.2. *Nearby Stellar Absorption Lines*

There are a number of weak stellar absorption lines surrounding Na I D (see, e.g., the high-resolution solar spectrum of Beckers, Bridges, & Gilliam 1976). These nearby stellar features introduce errors in continuum normalization and identification of blueshifted features.

For illustration, we compare the high-resolution population synthesis models of (González Delgado et al. 2005) to our observations of two galaxies (Figure 7). We use two composite models, created with the Sed@.0 code⁴, to bracket the expected range of stellar Na I D in our spectra. We have combined a 40 Myr old single stellar population (instantaneous burst) model with a 10 Gyr old model, to represent the starburst and the old underlying population, respectively (40 Myr reflects the gas consumption time in infrared-luminous galaxies). The two models have solar metallicity and young/old stellar mass fractions of 10/90 and 1/99. In the 1/99 model, the luminosities of the two populations are comparable, and the old population dominates the equivalent width of Na I D (which is strongest in old, cool stars). In the 10/90 model, the young population dominates the luminosity of the galaxy and the Na I D feature is weaker. We boxcar smooth our data to $\sim 150 \text{ km s}^{-1}$, and convolve the models with a $\sigma = 200 \text{ km s}^{-1}$ Gaussian (similar to the measured circular velocity of ULIRGs; K. Dasyra, private communication). The models are normalized to unity at 5910 \AA (just redward of Na I D), and we add a linear normalization of $-6 \times 10^{-4} \text{ \AA}^{-1}$ to match the data.

The strongest nearby stellar feature is located 33 \AA (1700 km s^{-1}) blueward of the D_2 line and is centered at 5857.5 \AA . There is variation in its strength among our spectra, and in general it is only noticeable after smoothing and too far to the blue to mimic anything but very high velocity outflowing gas. For instance, in F10378+1108 (Figure 7b), this stellar feature blends slightly with the most blueshifted interstellar component, but the stellar contribution is small. A secondary stellar feature (arising primarily from young stars) is closer in wavelength to Na I D but weaker, and an examination of our spectra shows that it

⁴See <http://www.iaa.es/rosa/> for the models and <http://www.iaa.es/~mcs/sed@> for code documentation.

has little or no impact on our results.

Though these weak, blueshifted stellar features are present in most galaxies, they are either too blueshifted or too weak to affect our fitting in cases where a wind is present. Thus, we consider this source of error to be small. However, spectra with apparent high-velocity, blueshifted interstellar lines must still be carefully inspected to ensure that these lines are not stellar in origin.

The best way to remove the effect of blueshifted stellar lines would be to fit stellar population synthesis models to our data and remove this component. However, our spectra are in general not of high enough signal-to-noise to do this reliably. To minimize errors in continuum fitting, we have generally avoided the strongest stellar features blueward of Na I D.

6.3.3. *Stellar Contribution to Na I D*

In galaxy spectra, Na I D has contributions due to stellar absorption from late type stars and interstellar absorption from clouds of gas. Figure 7 illustrates this. In one galaxy (F15549+4201), the Na I D absorption is purely stellar (consistent with our fitting and the absence of an outflow; see Paper II). In the other (F10378+1108), the absorption is mostly interstellar, but there is some stellar contribution. In a re-analysis of our data for this object, we are able to fit a weak, optically thick line at the position of the stellar absorption, plus three blueshifted interstellar components (though we do not ultimately use this fit, as it is unconstrained; see Paper II).

We can estimate the expected stellar contribution to Na I D by scaling the equivalent width of the Mg I *b* triplet, $\lambda\lambda 5167, 5173, 5185$ (Heckman et al. 2000; Rupke et al. 2002). This is possible because of the similar mechanisms by which Na and Mg are created in stars and their similar first ionization potentials (5.14 eV for Na, 7.65 eV for Mg). There is thus a correlation between the stellar equivalent widths of Mg I *b* and Na I D in galaxy spectra. Using a small sample of optically bright, nearby galaxies from Heckman, Balick, & Crane (1980), we infer that $W_{eq}^*(\text{Na I D}) = 0.5 \times W_{eq}(\text{Mg I } b)$. A fit gives a coefficient of 0.75, but we estimate instead the envelope of the data. This is more appropriate if we assume that excess Na I D absorption is interstellar in origin. With this correlation, the median stellar contribution to $W_{eq}(\text{Na I D})$ is 10% (i.e., insignificant) for galaxies with outflows in our sample.

To understand the relationship between $W_{eq}(\text{Mg I } b)$ and $W_{eq}(\text{Na I D})$ in infrared-luminous galaxies, we plot in Figure 8a $W_{eq}(\text{Mg I } b)$ vs. $W_{eq}(\text{Na I D})$ for a large sample of

galaxies. For each galaxy, the measured equivalent widths of Mg I *b* and Na I D are taken from the same source, either our spectra or low-dispersion spectra (Kim et al. 1995; Veilleux et al. 1999a; Heckman et al. 1980). (From our spectra, we measure $W_{eq}(\text{Mg I } b)$ using the smallest wavelength range that encompasses the three lines of the triplet.) The upper dashed line represents the expected stellar contribution to $W_{eq}(\text{Na I D})$. The fact that most points fall well below this line shows that the interstellar contribution is dominant in LIRGs and ULIRGs. This is expected given the large amounts of gas and dust in these galaxies.

Could the relative equivalent widths of Na I D and Mg I *b* be a good indicator of the presence of winds in these galaxies? Heckman et al. (2000) found this to be the case, in that those galaxies where the interstellar part of Na I D dominated were more likely to host winds. Figure 8*b* shows $W_{eq}(\text{Mg I } b)$ vs. $W_{eq}(\text{Na I D})$ for our sample galaxies for those cases where $W_{eq}(\text{Mg I } b)$ is present in our spectra or is available from other sources. The lower line in this plot is $W_{eq}(\text{Na I D}) = 3 \times W_{eq}(\text{Mg I } b)$. We find that most of the galaxies below this line have winds (80%), while only a small fraction above this line have winds (25%). This detection criterion is independent of star formation rate, as roughly the same percentages apply to each subsample taken separately. We thus agree with Heckman et al. (2000) and quantify this relationship. (See Paper II for more information on how the presence of a wind is determined.)

7. COMPUTATION OF COLUMN DENSITIES

Our data constrain the amount of ground-state Na present in the line-of-sight, which for a Maxwellian velocity distribution is proportional to the optical depth and the Doppler parameter *b* (Spitzer 1978):

$$N(\text{Na I}) = \frac{\tau_{1,c} b}{1.497 \times 10^{-15} \lambda_1 f_1}, \quad (10)$$

where f_1 , λ_1 , and $\tau_{1,c}$ are the oscillator strength, wavelength (in vacuum, in the rest frame), and central optical depth of the Na I D₁ $\lambda 5896$ line. (The units of $N[\text{Na I}]$, λ_1 , and b are cm^{-2} , \AA , and km s^{-1} , respectively.) Morton (1991) gives $f_1 = 0.3180$ and $\lambda_1 = 5897.55 \text{ \AA}$.

Since we are more interested in the total amount of hydrogen, we must correct for ionization to determine the total amount of Na, and then for depletion and non-solar abundances to get the amount of hydrogen. One way to do this is with an empirical calibration between $\log[N(\text{Na I})]$ and $\log[N(\text{H})]$, taken from local Galactic lines-of-sight. This was the approach in our preliminary report (Rupke et al. 2002). However, for the full sample we have chosen to do the ionization, depletion, and abundance corrections separately, both for clarity and

to allow us to apply corrections that depend on galaxy properties. The resulting formula is

$$N(\text{H}) = N(\text{Na I})(1 - y)^{-1}10^{-(a+b)} \quad (11)$$

where the column densities are in cm^{-2} , y is the ionization fraction, $a = \log[N(\text{Na})/N(\text{H})]_{gal}$ is the Na abundance in the galaxy of interest, and $b = \log[N(\text{Na})/N(\text{H})] - \log[N(\text{Na})/N(\text{H})]_{gal}$ is the depletion onto dust. We now discuss the values we use for each of these quantities.

7.1. Ionization State

The ionization state of the absorbing gas has the potential to be a significant uncertainty in converting $N(\text{Na I})$ to $N(\text{H})$. Na is easily ionized due to its low first ionization potential, 5.14 eV. Most or all of the Na in the vicinity of high-velocity shocks will be out of the ground state (see Sutherland & Dopita 1993 for the ionization structure of cooling, post-shock Na, and Dopita & Sutherland 1996 for the ionization structure of various elements in the shock and its precursor). Given the large amount of Na I that we observe, more plausible locations for the absorbing gas are either (a) the center of cold clouds/filaments that have been entrained and accelerated by the wind but not destroyed completely or (b) postshock regions where the gas has cooled sufficiently and recombined, and is no longer dominated by collisions or the hard shock radiation field. In the former case, we expect that these clouds will have ionized skins of warm and hot gas that are heated by the surrounding wind fluid.

Complicating this is the fact that without significant amounts of dust, Na may be ionized even in regions where hydrogen is neutral. This occurs in Mg I (which has a slightly larger first ionization potential, 7.65 eV) because (a) it has a low first IP compared to that of hydrogen and (b) there is a decrease in recombination with the drop in electron density in regions of neutral hydrogen (de Kool et al. 2001). In fact, if significant near-UV radiation ($\lambda \lesssim 3060 \text{ \AA}$) penetrates to the center of the clouds/filaments or post-shock regions of the wind, Na will still be highly ionized. We do know that there is dust in these winds based on the correlation of $E(B-V)$ and the equivalent width of Na I D seen in LIRGs and ULIRGs (Veilleux et al. 1995; Kim et al. 1998), and this dust may shield the neutral Na I D atoms and prevent total ionization.

For our galaxies, we assume modest ionization, with $N(\text{Na})/N(\text{Na I}) = 10$. This is in the middle of the range of ionization corrections set by an empirical conversion from Na to H, as determined by measurements along sightlines toward Galactic stars (Stokes 1978). It also matches the ionization fraction of a cold H I cloud in NGC 3067 (Stocke et al. 1991); this cloud is in the galaxy’s halo, where we expect much of the blueshifted absorption to arise in our sample.

Our column densities (and subsequent masses, momenta, and energies) scale inversely with the values we assume for the ionization fraction [$y = 1 - N(\text{Na I})/N(\text{Na}) = 0.9$]. If this number is at all incorrect, it is likely to increase, since the environments of these clouds are governed by turbulent shocks. Increasing the ionization fraction will increase our measured values of mass, momentum, energy, and mass entrainment efficiency (Paper II).

7.2. Metallicity

It is a well-established fact that the metallicity and luminosity (or mass) of galaxies are correlated (see Garnett 2002, and references therein). This correlation could in fact be explained by superwinds if more massive galaxies retain their metals more efficiently than lower mass galaxies (e.g., Bregman 1978; Kauffmann & Charlot 1998; van den Bosch 2002). We apply the luminosity-metallicity relation to our sample to determine metallicities for individual galaxies. However, for the four dwarf galaxies used in Paper II, we instead use the observed metallicities listed in Schwartz & Martin (2004).

The luminosity-metallicity relation we use is measured in the near-infrared (Salzer et al. 2005). The advantage of using near-infrared data is that it is less sensitive to dust effects (which are important in our sample) and is a better probe of mass than optical data. Because K -band magnitudes are available for almost all the galaxies in our sample, we use the functional dependence of $\log[N(\text{O})/N(\text{H})]$ on M_K (where metallicity is calculated from the Edmunds & Pagel 1984 R_{23} relation; Salzer et al. 2005). We assume that the relation flattens above the luminosity $M_K = -25$; such a flattening is observed in the optical (Tremonti et al. 2004). This threshold is based on the assumption that the flattening occurs just out of range of the data of Salzer et al. (2005). Using values from Savage & Sembach (1996) for $\log[N(\text{O})/N(\text{H})]_{\odot}$ ($= -3.13$) and $\log[N(\text{Na})/N(\text{H})]_{\odot}$ ($= -5.69$), the resulting equation for the Na abundance in a galaxy with $M_K > -25$ is

$$\log[N(\text{Na})/N(\text{H})]_{gal} = -10.647 - (0.212M_K). \quad (12)$$

If $M_K \leq -25$, then $\log[N(\text{Na})/N(\text{H})]_{gal} = -5.347$. Using this relation, we find that the galaxies in our sample have twice solar metallicity on average. (For the handful of galaxies without K -band measurements, we assume this mean metallicity.)

For depletion of Na atoms onto dust, we use the canonical Galactic value of -0.95 (Savage & Sembach 1996).

8. SUMMARY

In this paper we introduce our sample of 78 starburst-dominated, infrared-luminous galaxies. We discuss the sample selection and important properties of the galaxies (redshift, luminosity, mass, spectral type). We present our data reduction procedures in brief. The spectrum of Na I D in each galaxy is shown. The equations for computing Na I and H column densities from the data are presented. Finally, we discuss at length our fitting procedures and the subtleties of measuring the absorption-line parameters. Our absorption lines are blended doublets observed at moderately high resolution, a case that has not been addressed in the literature in detail. One important finding is that the doublet ratio method is invalid if, after fitting Gaussian intensity profiles, the optical depth is found to be large, since this violates the assumptions of the method. A better method for resolved but blended data is to fit more complex intensity profiles that are functions of physical parameters (velocity, optical depth, and covering fraction).

A detailed analysis of these data is presented in Paper II (Rupke et al. 2005a).

We thank Kalliopi Dasyra and Dong Chan Kim for supplying useful data prior to publication. DSR is supported by NSF/CAREER grant AST-9874973. SV is grateful for partial support of this research by a Cottrell Scholarship awarded by the Research Corporation, NASA/LTSA grant NAG 56547, and NSF/CAREER grant AST-9874973. This research has made use of the NASA/IPAC Extragalactic Database (NED), which is operated by JPL/Caltech, under contract with NASA. It also makes use of data products from the Two Micron All Sky Survey, which is a joint project of the University of Massachusetts and IPAC/Caltech, funded by NASA and NSF. The authors wish to recognize and acknowledge the very significant cultural role and reverence that the summit of Mauna Kea has always had within the indigenous Hawaiian community. We are most fortunate to have the opportunity to conduct observations from this mountain.

A. APPENDIX: COMMENTS ON INDIVIDUAL OBJECTS

Here we discuss unique properties of individual galaxies based on our spectra and publicly available red DSS2 and 2MASS images.

- **F01417+1651 (III Zw 35)**. The spectral types of the two nuclei listed in Veilleux et al. (1995) are backwards.

- **F02509+1248 (NGC 1134)**. This galaxy has no spectral type in the literature, and we do not observe the [O III] $\lambda 5007$ line in this galaxy. However, Condon, Cotton, & Broderick (2002) classify it as a starburst on the basis of (1) the radio/FIR flux ratio, (2) the $25\mu\text{m}/60\mu\text{m}$ flux ratio, and (3) a lack of extended radio structures.
- **F02512+1446**. Zink et al. (2000) and Surace, Sanders, & Mazzarella (2004) show that the southern nucleus is the source of the far-infrared emission. The northern nucleus in this galaxy contains no emission lines. It does, however, contain blueshifted Na I D gas in its spectrum that is at the redshift of the southern nucleus, suggesting that the S nucleus is in the foreground. If we assume this, and also that the redder Na I D component in this galaxy is the stellar systemic velocity, we compute a redshift for the N nucleus of 0.0324.
- **F1_5**. This galaxy is the only one in our sample without *IRAS* fluxes. (The apparent peaks in the 60 and 100 μm flux maps are from another nearby IR source.) It does have an *ISO* 12 μm flux, and its bolometric luminosity is estimated using a starburst SED (Clements et al. 1999, 2001). This is clearly only a zeroth-order estimate of L_{IR} , but we have kept it in our sample due to its high redshift and the beautiful, high S/N Na I D profile evident in its spectrum.
- **F04326+1904 (UGC 3094)**. This galaxy has no spectral type in the literature, and we do not observe the [O III] $\lambda 5007$ line in this galaxy. However, Condon et al. (2002) classify it as a starburst on the basis of (1) the radio/FIR flux ratio, (2) the $25\mu\text{m}/60\mu\text{m}$ flux ratio, and (3) a lack of extended radio structures.
- **F07353+2903**. There is an emission-line object located $\lesssim 2''$ south of the galaxy center. We detect an emission line at 8704.3 \AA . If we assume it is [O III] $\lambda 5007$, [O III] $\lambda 4959$ is detected with modest significance at the expected location, and $\text{H}\beta$ with low significance. If these line identifications are correct, the redshift of the object is 0.7380, and it is likely to be an AGN based on the flux ratio of [O III] $\lambda 5007$ and $\text{H}\beta$.
- **F08143+3134**. $\text{H}\alpha$ and [N II] in this galaxy are blended and have strong blue wings; deblending them is thus non-trivial. However, [O III] $\lambda 5007/\text{H}\beta \sim 1.6$, which implies that the spectral type is H II or LINER.
- **F08591+5248**. This galaxy has no spectral classification listed in Veilleux et al. (1999a), and we cannot classify it because $\text{H}\alpha$ intersects telluric lines. An unpublished low-dispersion spectrum of this object (from another project) shows that [O III] $\lambda 5007/\text{H}\beta \sim 0.8$, which implies it is either an H II galaxy or a LINER.

- **F09039+0503.** The narrow absorbing component in this galaxy observed in Na I D at $+190 \text{ km s}^{-1}$ is observed also in Ca II K at the same velocity.
- **F10565+2448.** This galaxy has a bright central object with one or more nearby nuclei that are interacting with the central object. For the central object, we measure an optical emission-line redshift of $v_{hel} = 12891 \text{ km s}^{-1}$, and the outflowing components appear in Na I D at 12758 and 12590 km s^{-1} . Our systemic redshift is in good agreement with the RC3 heliocentric optical redshift of $12912 \pm 37 \text{ km s}^{-1}$, the CO redshifts of 12895 km s^{-1} (Sanders et al. 1991) and $v_{lsr} = 12923 \text{ km s}^{-1}$ (Downes & Solomon 1998), and the deepest H I 21 cm trough at 12900 km s^{-1} . However, these differ from the optical redshifts listed in Kim et al. (1995), which are 13160 km s^{-1} for the central object and 13100 km s^{-1} for the fainter NE nucleus.
- **F11387+4116.** There is a background emission-line object $3''.8$ south of the galaxy; no continuum is visible, but [O III] $\lambda 5007$, H β , and H α are observed, yielding $z = 0.346$. This background emission-line object has [O III]/H $\beta > 3$ (suggesting the presence of an AGN).
- **F16474+3430.** We do not have individual [O III] $\lambda 5007$ fluxes for the two nuclei in this galaxy. From Veilleux et al. (1999a), [O III]/H $\beta \sim 1$ for one of the nuclei or both together. We assume that this ratio is small for both nuclei to achieve our nuclear classifications (H II for each case).
- **F21549–1206.** The redshift listed in Kim et al. (1995) for the SE nucleus in this source is incorrect; its redshift is 0.0900 , not 0.051 . Thus the SE nucleus is a distant background galaxy.

REFERENCES

- Aguirre, A., Hernquist, L., Schaye, J., Katz, N., Weinberg, D. H., & Gardner, J. 2001a, ApJ, 561, 521
- Aguirre, A., Hernquist, L., Schaye, J., Weinberg, D. H., Katz, N., & Gardner, J. 2001b, ApJ, 560, 599
- Aguirre, A., Schaye, J., Hernquist, L., Kay, S., Springel, V., & Theuns, T. 2005, ApJ, 620, L13
- Arav, N., Becker, R. H., Laurent-Muehleisen, S. A., Gregg, M. D., White, R. L., Brotherton, M. S., & de Kool, M. 1999, ApJ, 524, 566

- Arav, N., Kaastra, J., Steenbrugge, K., Brinkman, B., Edelson, R., Korista, K. T., de Kool, M. 2003, *ApJ*, 590, 174
- Arav, N., Korista, K. T., de Kool, M., Junkkarinen, V. T., & Begelman, M. 1999, *ApJ*, 516, 27
- Armus, L., Heckman, T. M., & Miley, G. K. 1990, *ApJ*, 364, 471
- Arribas, S., Bushouse, H., Lucas, R. A., Colina, L., & Borne, K. D. 2004, *AJ*, 127, 2522
- Barger, A. J., Cowie, L. L., & Sanders, D. B. 1999, *ApJ*, 518, L5
- Barlow, T. A., & Sargent, W. L. W. 1997, *AJ*, 113, 136
- Beckers, J. M., Bridges, C. A., & Gilliam, L. B. 1976, *A High Resolution Spectral Atlas of the Solar Irradiance From 380 to 700 Nanometers. Volume I. Tabular Form* (Massachusetts: Air Force Geophysics Lab)
- Blain, A. W., Barnard, V. E., & Chapman, S. C. 2003, *MNRAS*, 338, 733
- Blain, A. W., Kneib, J.-P., Ivison, R. J., & Smail, I. 1999, *ApJ*, 512, L87
- Bregman, J. N. 1978, *ApJ*, 224, 768
- Buote, D. A. 2000, *ApJ*, 539, 172
- Chapman, S. C., Blain, A. W., Ivison, R. J., & Smail, I. R. 2003, *Nature*, 422, 695
- Chevalier, R. A., & Clegg, A. W. 1985, *Nature*, 317, 44
- Clements, D. L., Desert, F.-X., & Franceschini, A. 2001, *MNRAS*, 325, 665
- Clements, D. L., Desert, F.-X., Franceschini, A., Reach, W. T., Baker, A. C., Davies, J. K., & Cesarsky, C. 1999, *A&A*, 346, 383
- Cole, S., Lacey, C. G., Baugh, C. M., & Frenk, C. S. 2000, *MNRAS*, 319, 168
- Condon, J. J., Anderson, M. L., & Helou, G. 1991, *ApJ*, 378, 65
- Condon, J. J., Cotton, W. D., & Broderick, J. J. 2002, *AJ*, 124, 675
- Cowie, L. L., Barger, A. J., Fomalont, E. B., & Capak, P. 2004, *ApJ*, 603, L69
- de Kool, M., Arav, N., Becker, R. H., Gregg, M. D., White, R. L., Laurent-Muehleisen, S. A., Price, T., & Korista, K. T. 2001, *ApJ*, 548, 609

- Dopita, M. A., & Sutherland, R. S. 1996, *ApJS*, 102, 161
- Downes, D., & Solomon, P. M. 1998, *ApJ*, 507, 615
- Edmunds, M. G., & Pagel, B. E. J. 1984, *MNRAS*, 211, 507
- Garnett, D. R. 2002, *ApJ*, 581, 1019
- Genzel, R., et al. 1998, *ApJ*, 498, 579
- Genzel, R., Tacconi, L. J., Rigopoulou, D., Lutz, D., & Tecza, M. 2001, *ApJ*, 563, 527
- González Delgado, R. M., Cerviño, M., Martins, L. P., Leitherer, C., & Hauschildt, P. H. 2005, *MNRAS*, 357, 945
- Hamann, F., Barlow, T. A., Junkkarinen, V., & Burbidge, E. M. 1997, *ApJ*, 478, 80
- Heckman, T. M., Balick, B., & Crane, P. C. 1980, *A&AS*, 40, 295
- Heckman, T. M., Lehnert, M. D., Strickland, D. K., & Armus, L. 2000, *ApJS*, 129, 493
- Horne, K. 1986, *PASP*, 98, 609
- Hughes, D. H., et al. 1998, *Nature*, 394, 241
- Hutchings, J. B. 1989, *AJ*, 98, 524
- Ishida, C. M. 2004, PhD dissertation, University of Hawaii
- Jarrett, T. H., Chester, T., Cutri, R., Schneider, S., & Huchra, J. 2003, *AJ*, 125, 525
- Jenkins, E. B. 1986, *ApJ*, 304, 739
- Kauffmann, G., & Charlot, S. 1998, *MNRAS*, 294, 705
- Kennicutt, R. C. 1998, *ApJ*, 498, 541
- Kewley, L. J., Heisler, C. A., Dopita, M. A., & Lumsden, S. 2001, *ApJS*, 132, 37
- Kim, D.-C., & Sanders, D. B. 1998, *ApJS*, 119, 41
- Kim, D.-C., Sanders, D. B., Veilleux, S., Mazzarella, J. M., & Soifer, B. T. 1995, *ApJS*, 98, 129
- Kim, D.-C., Veilleux, S., & Sanders, D. B. 1998, *ApJ*, 484, 92
- Kim, D.-C., Veilleux, S., & Sanders, D. B. 2002, *ApJS*, 143, 277

- Kriss, G. A. 1994, in ASP Conf. Ser. 61, ADASS III, ed. D. R. Crabtree, R. J. Hanisch, & J. Barnes (San Francisco: ASP), 437
- Laor, A., & Brandt, W. N. 2002, ApJ, 569, 641
- Lehnert, M. D., & Heckman, T. M. 1995, ApJS, 97, 89
- Lehnert, M. D., & Heckman, T. M. 1996, ApJ, 462, 651
- Lilly, S. J., Eales, S. A., Gear, W. K. P., Hammer, F., Le Fèvre, O., Crampton, D., Bond, J. R., & Dunne, L. 1999, ApJ, 518, 641
- Lutz, D., Veilleux, S., & Genzel, R. 1999, ApJ, 517, L13
- Madau, P., Ferrara, A., & Rees, M. J. 2001, ApJ, 555, 92
- Marsh, T. 1989, PASP, 100, 1032
- Martin, C. L. 2005, ApJ, 621, 227
- Martin, J. M., Bottinelli, L., Dennefeld, M., & Gouguenheim, L. 1991, A&A, 245, 393
- Mirabel, I. F., & Sanders, D. B. 1988, ApJ, 335, 104
- Morton, D. C. 1991, ApJS, 77, 119
- Murphy, T. W., Jr., Soifer, B. T., Matthews, K., & Armus, L. 2001, ApJ, 559, 201
- Nachmann, P., & Hobbs, L. M. 1973, ApJ, 182, 481
- Nagar, N. M., Wilson, A. S., Falcke, H., Veilleux, S., & Maiolino, R. 2003, A&A, 409, 115
- Perez-Gonzalez, P. G., et al. 2005, ApJ, in press (astro-ph/0505101)
- Phillips, A. C. 1993, AJ, 105, 486
- Press, W. H., Teukolsky, S. A., Vetterling, W. T., & Flannery, B. P. 1992, Numerical Recipes in C (New York: Cambridge)
- Renzini, A. 1997, ApJ, 488, 35
- Rupke, D. S., Veilleux, S., & Sanders, D. B. 2002, ApJ, 570, 588
- Rupke, D. S., Veilleux, S., & Sanders, D. B. 2005a, ApJ, in press
- Rupke, D. S., Veilleux, S., & Sanders, D. B. 2005b, ApJ, in press

- Salzer, J. J., Lee, J. C., Melbourne, J., Hinz, J. L., Alonso-Herrero, A., & Jangren, A. 2005, *ApJ*, 624, 661
- Sanders, D. B., & Mirabel, I. F. 1996, *ARA&A*, 34, 749
- Sanders, D. B., Mazzarella, J. M., Kim, D.-C., Surace, J. A., & Soifer, B. T. 2003, *AJ*, 126, 1607
- Sanders, D. B., Scoville, N. Z., & Soifer, B. T. 1991, *ApJ*, 370, 158
- Sanders, D. B., Soifer, B. T., Elias, J. H., Madore, B. F., Matthews, K., Neugebauer, G., & Scoville, N. Z. 1988, *ApJ*, 325, 74
- Savage, B. D., & Sembach, K. R. 1996, *ARA&A*, 34, 279
- Scannapieco, E., Thacker, R. J., & Davis, M. 2001, *ApJ*, 557, 605
- Schwartz, C. M., & Martin, C. L. 2004, *ApJ*, 610, 201
- Sheinis, A. I., Bolte, M., Epps, H. W., Kibrick, R. I., Miller, J. S., Radovan, M. V., Bigelow, B. C., & Sutin, B. M. 2002, *PASP*, 114, 851
- Silk, J. 2003, *MNRAS*, 343, 249
- Simcoe, R. A., Sargent, W. L. W., & Rauch, M. 2002, *ApJ*, 578, 73
- Smail, I., Ivison, R. J., & Blain, A. W. 1997, *ApJ*, 490, L5
- Solomon, P. M., Downes, D., Radford, S. J. E., & Barrett, J. W. 1997, *ApJ*, 478, 144
- Somerville, R. S., & Primack, J. R. 1999, *MNRAS*, 310, 1087
- Spitzer, L. 1968, *Diffuse Matter in Space* (New York: Wiley-Interscience)
- Spitzer, L. 1978, *Physical Processes in the Interstellar Medium* (New York: Wiley-Interscience)
- Springel, V., & Hernquist, L. 2003, *MNRAS*, 339, 289
- Stanford, S. A., Stern, D., van Breugel, W., & De Breuck, C. 2000, *ApJS*, 131, 185
- Stocke, J. T., Case, J., Donahue, M., Shull, J. M., & Snow, T. P. 1991, *ApJ*, 374, 72
- Stokes, G. M. 1978, *ApJS*, 36, 115
- Surace, J. A., Sanders, D. B., & Mazzarella, J. M. 2004, *AJ*, 127, 3235

- Sutherland, R. S., & Dopita, M. A. 1993, *ApJS*, 88, 253
- Tacconi, L. J., Genzel, R., Lutz, D., Rigopoulou, D., Baker, A. J., Iserlohe, C., & Tecza, M. 2002, *ApJ*, 580, 73
- Tremonti, C. A., et al. 2004, *ApJ*, 613, 898
- Theuns, T., Viel, M., Kay, S., Schaye, J., Carswell, R. F., & Tzanavaris, P. 2002, *ApJ*, 578, L5
- van den Bosch, F. C. 2002, *MNRAS*, 332, 456
- van Driel, W., Gao, Y., & Monnier-Ragaigne, D. 2001, *A&A*, 368, 64
- Veilleux, S., Cecil, G., & Bland-Hawthorn, J. 2005, *ARA&A*, in press (astro-ph/0504435)
- Veilleux, S., Kim, D.-C., & Sanders, D. B. 1999a, *ApJ*, 522, 113
- Veilleux, S., Kim, D.-C., & Sanders, D. B. 2002, *ApJ*, 143, 315
- Veilleux, S., Kim, D.-C., Sanders, D. B., Mazzarella, J. M., & Soifer, B. T. 1995, *ApJS*, 98, 171
- Veilleux, S., Sanders, D. B., & Kim, D.-C. 1999b, *ApJ*, 522, 139
- Veilleux, S., & Osterbrock, D. E. 1987, *ApJS*, 63, 295
- Veilleux, S., & Rupke, D. S. 2004, *PASA*, 21, 393
- Wainscoat, R. J., & Cowie, L. L. 1992, *AJ*, 103, 332
- Zink, E. C., Lester, D. F., Doppmann, G., & Harvery, P. M. 2000, *ApJS*, 131, 413

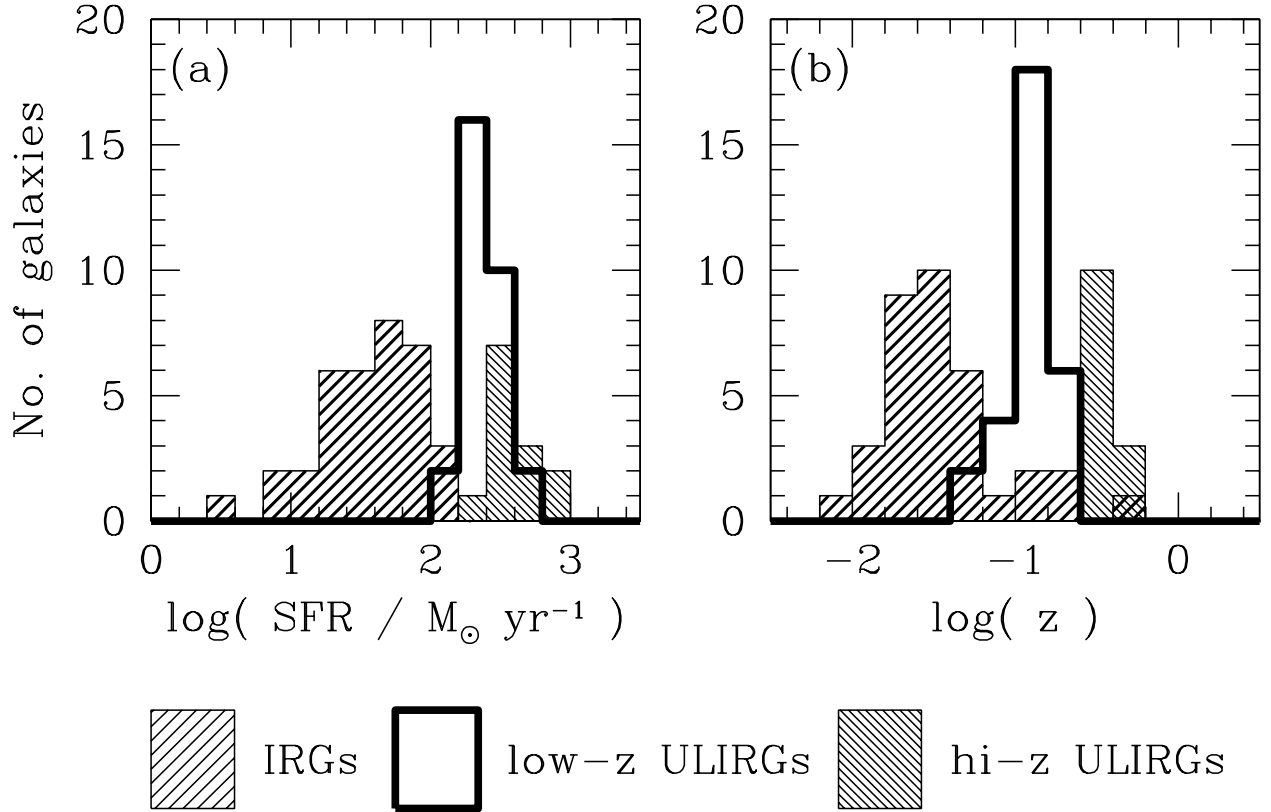


Fig. 1.— The distributions of (a) star formation rate and (b) redshift for our three subsamples. Note from (a) that the division in star formation rate (or equivalently, infrared luminosity; see §2) between the low-luminosity IRGs and the ULIRGs occurs at $\text{SFR} \sim 150 M_{\odot} \text{ yr}^{-1}$. The low- z and high- z ULIRGs are also divided at $z = 0.25$ (b). See §2 for the subsample definitions.

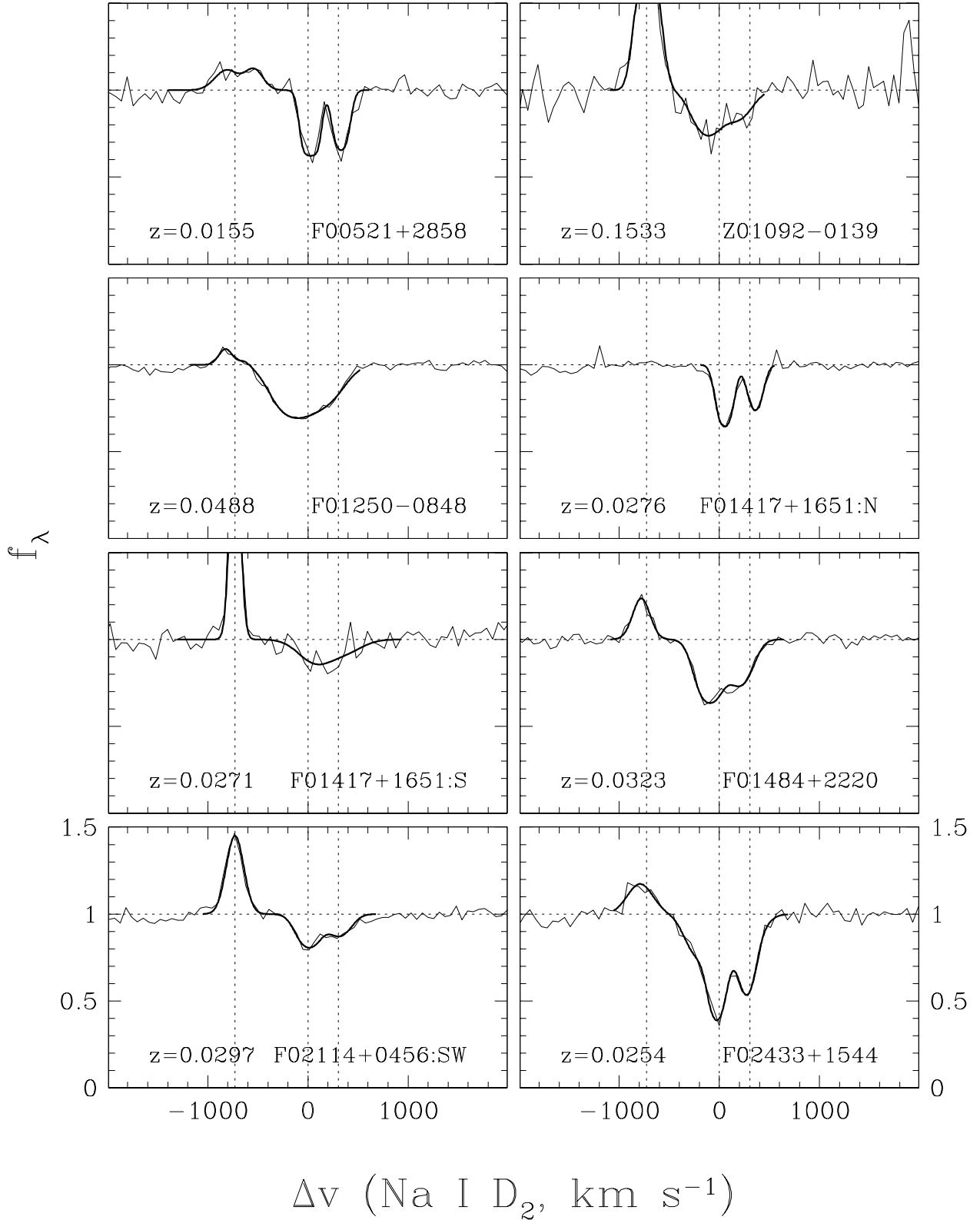


Fig. 2.— Spectra of the Na I D line in our IRG (low L_{IR}) subsample. The thin lines are the original spectra (slightly smoothed) and the thick lines are the fits to the data. The vertical dotted lines locate the Na I D $\lambda\lambda 5890, 5896$ doublet and He I $\lambda 5876$ emission line in the rest frame of the galaxy. The diagonal hashed lines locate atmospheric absorption from O₂, when present.

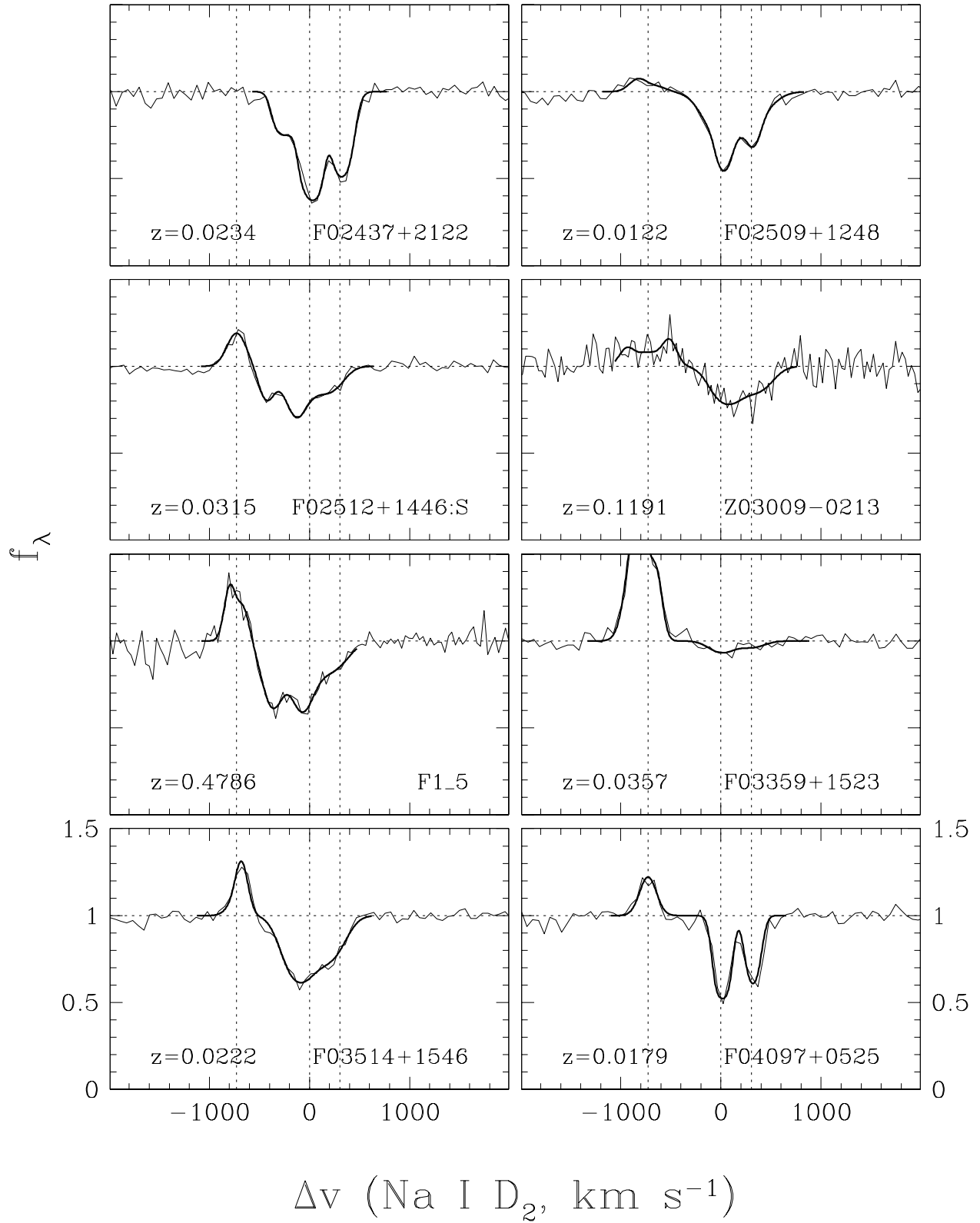


Fig. 2.— *Continued.*

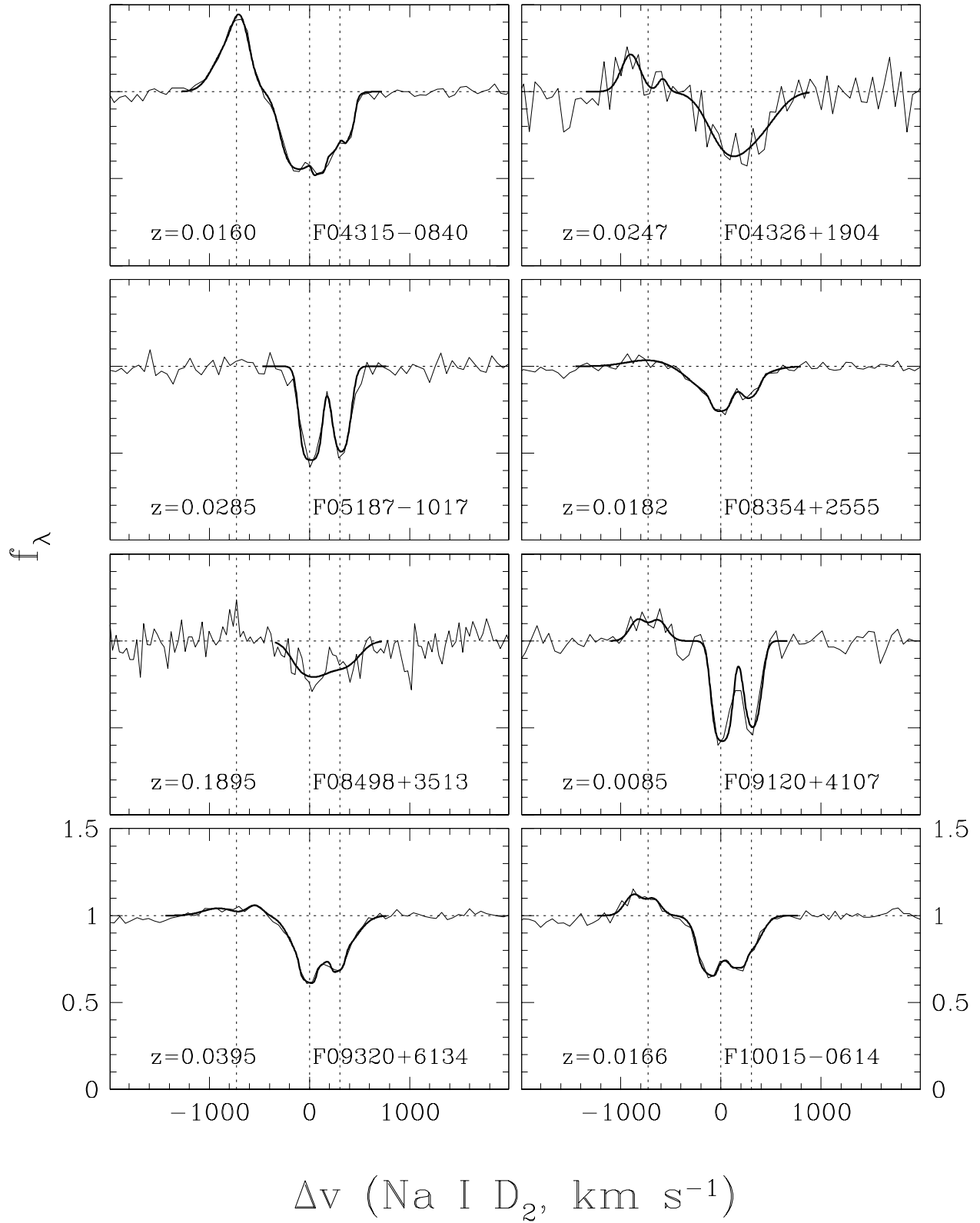


Fig. 2.— *Continued.*

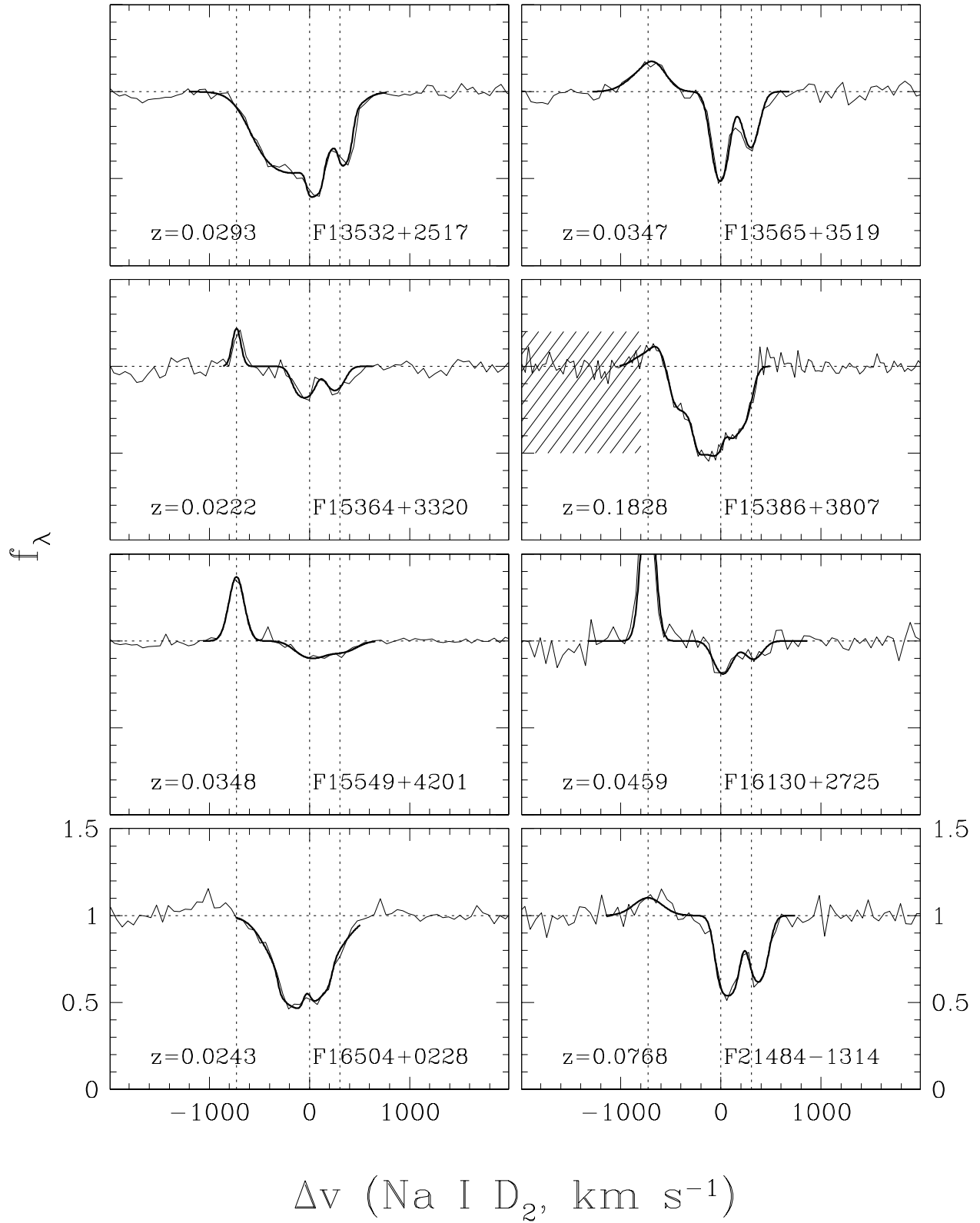


Fig. 2.— *Continued.*

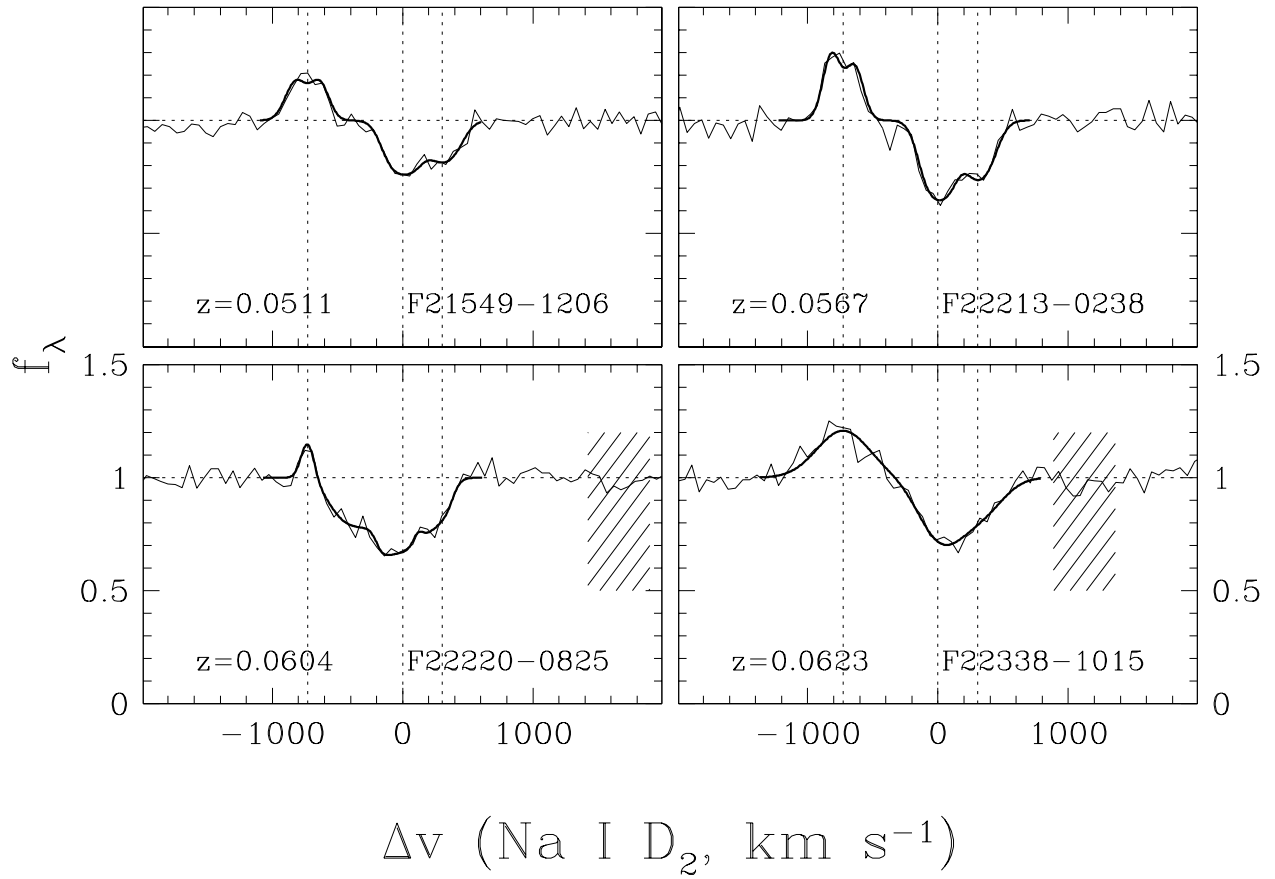


Fig. 2.— *Continued.*

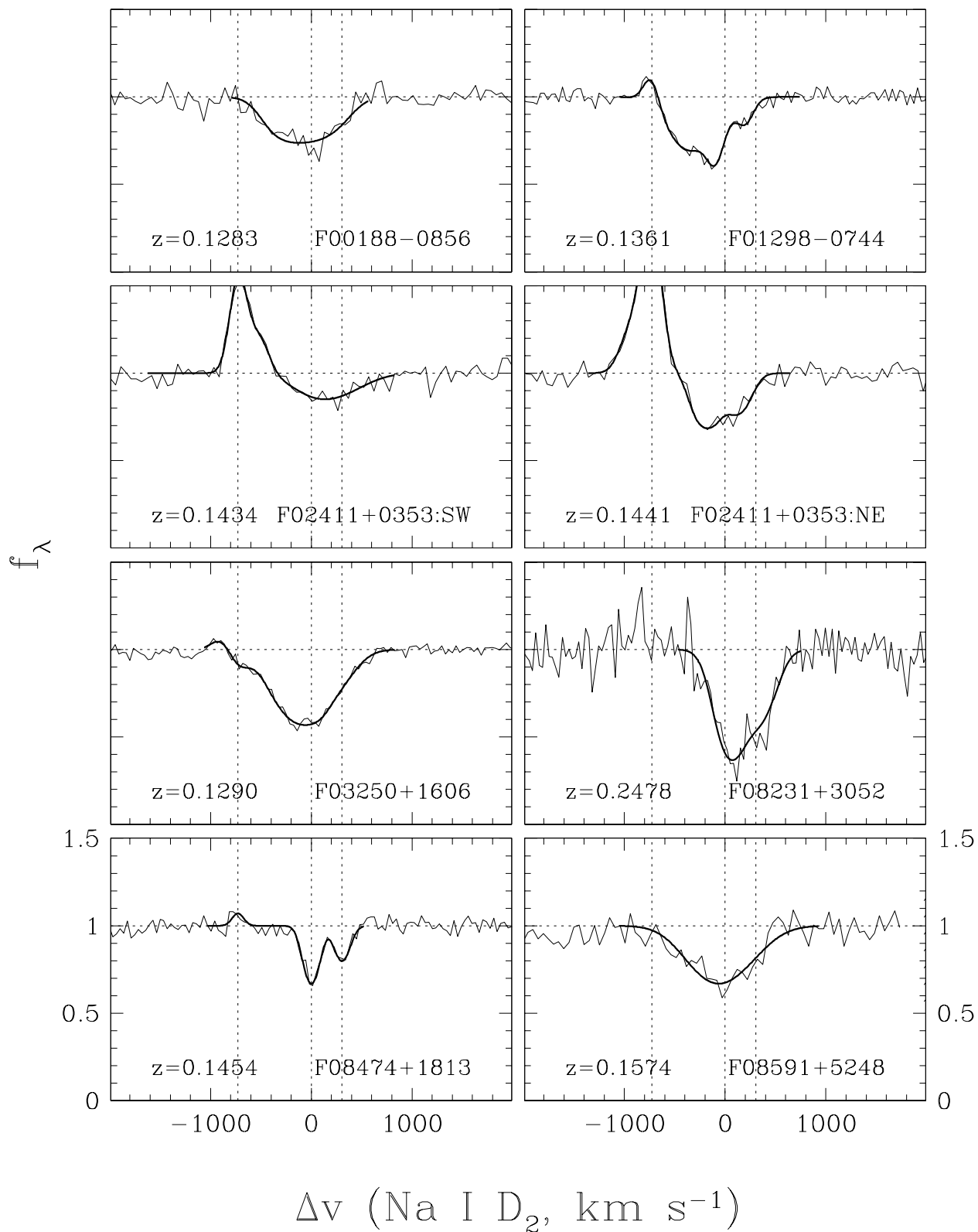


Fig. 3.— Spectra of the Na I D line in our $z < 0.25$ ULIRG subsample. See Figure 2 for more details.

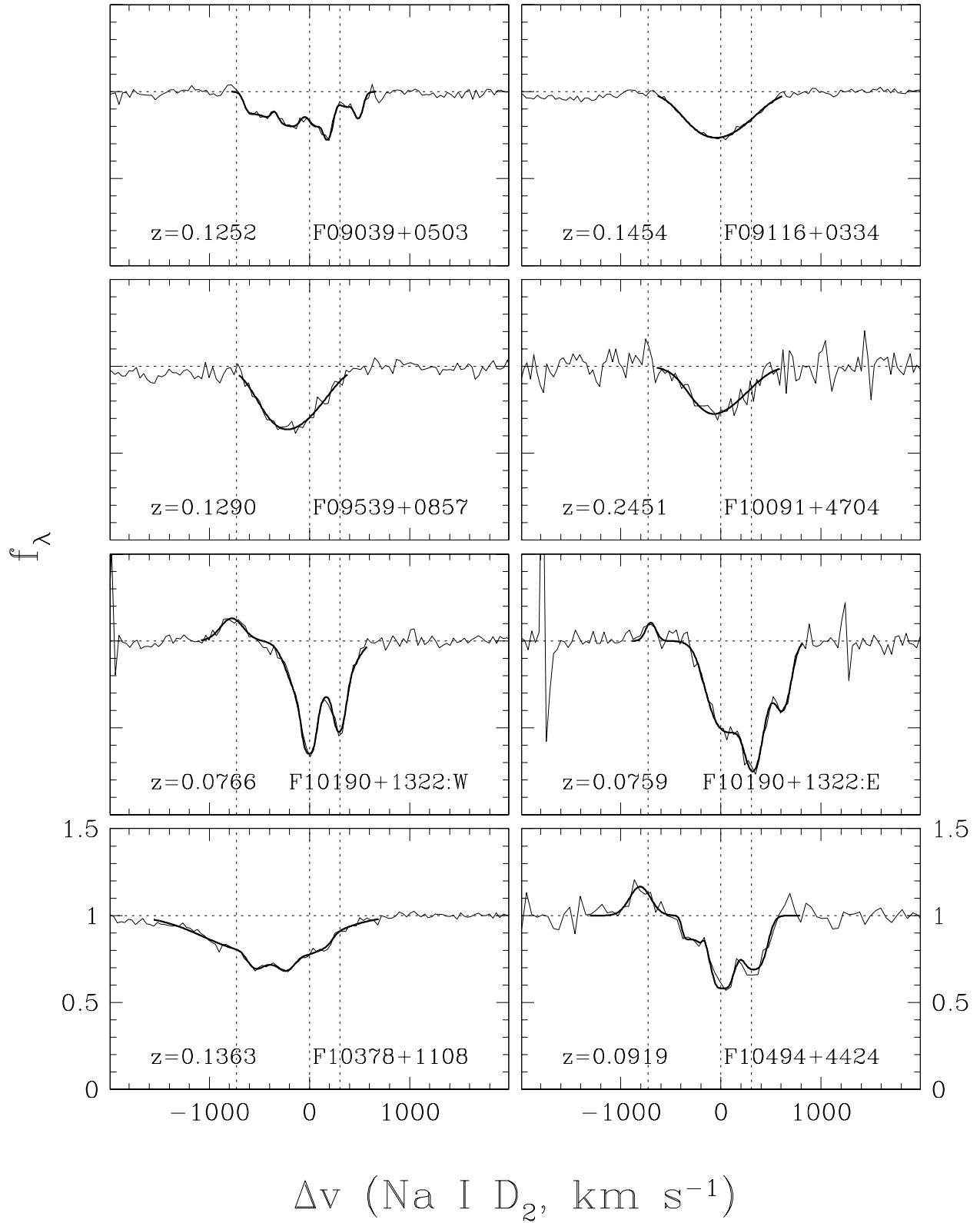


Fig. 3.— *Continued.*

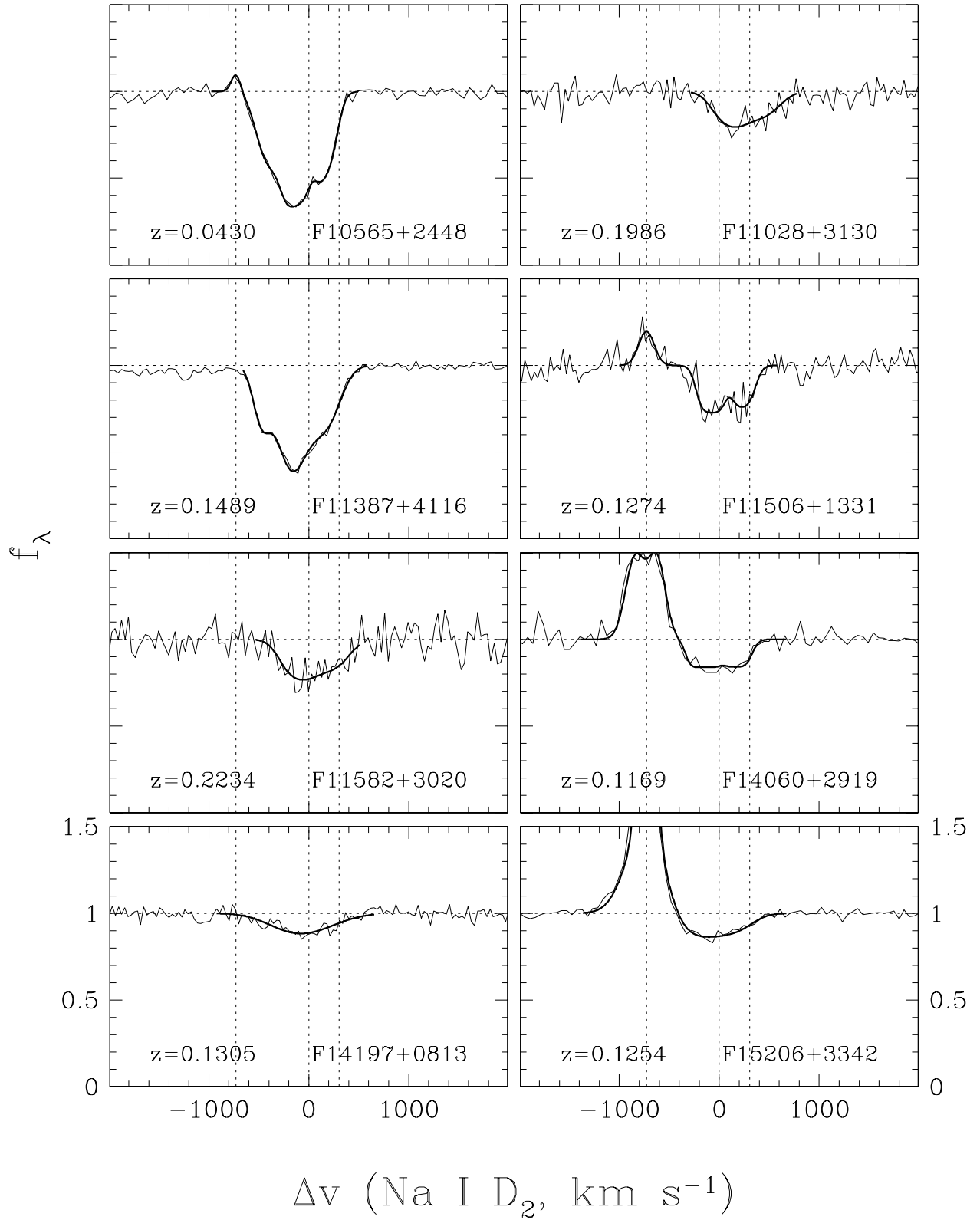


Fig. 3.— *Continued.*

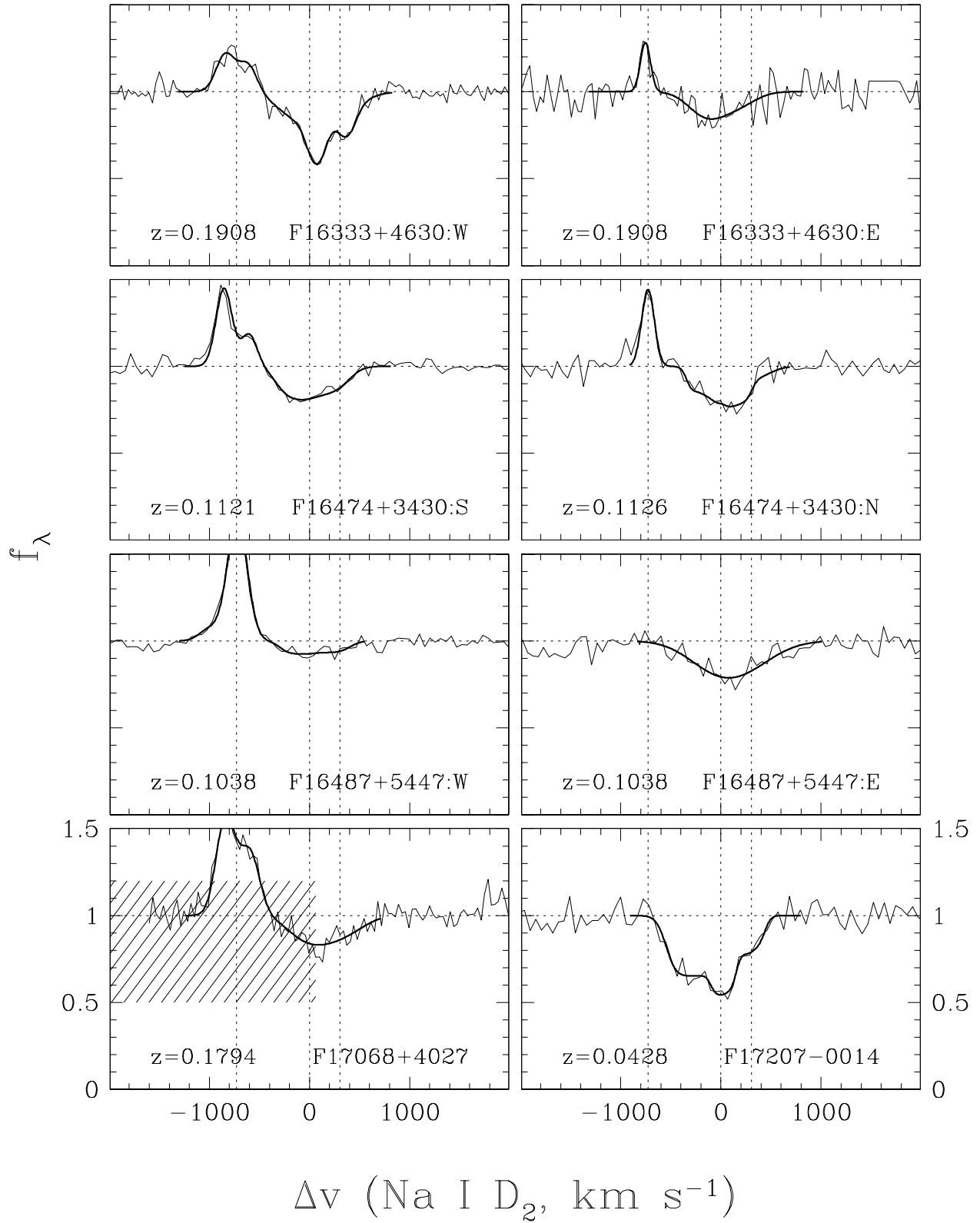


Fig. 3.— *Continued.*

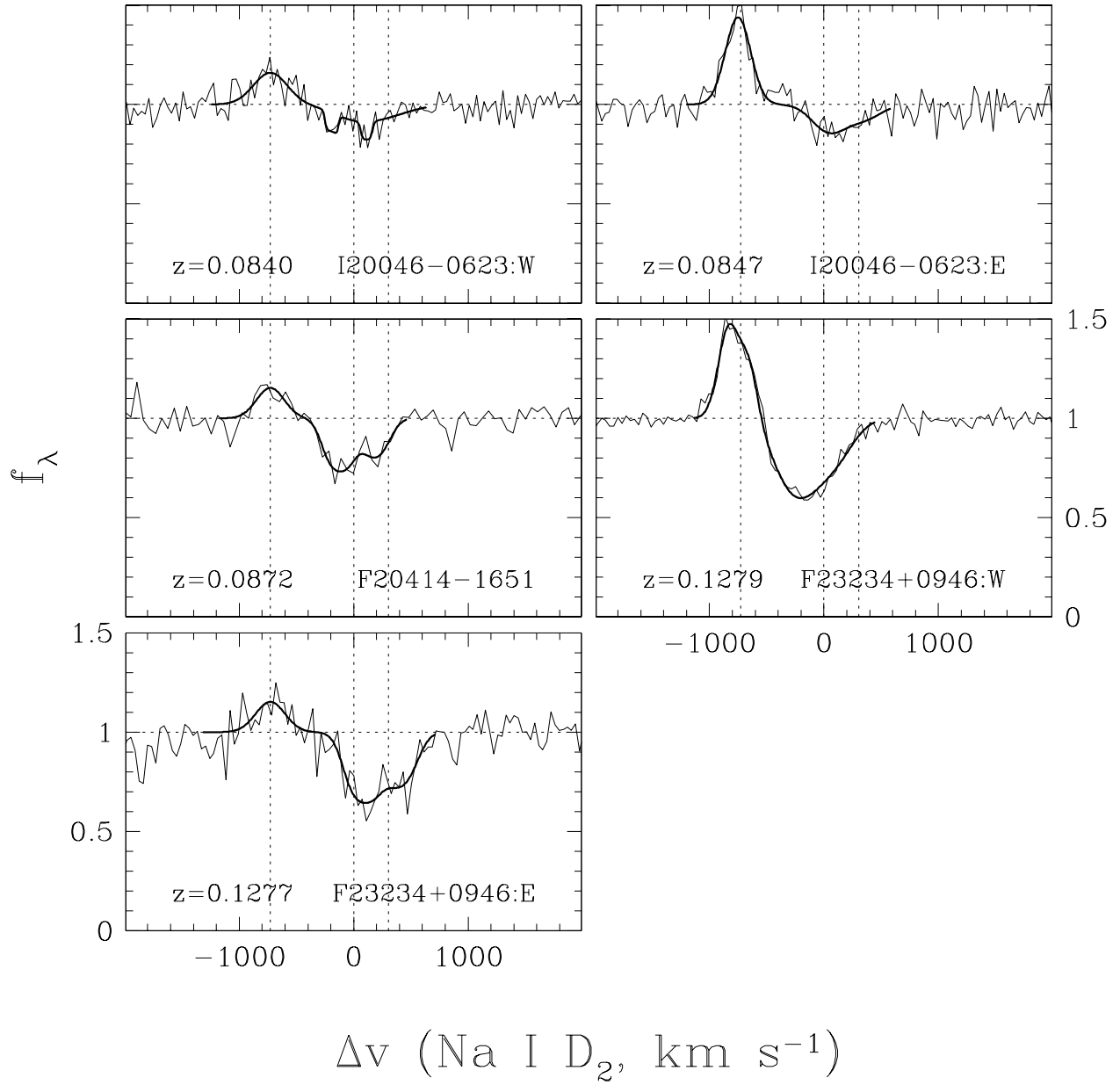


Fig. 3.— *Continued.*

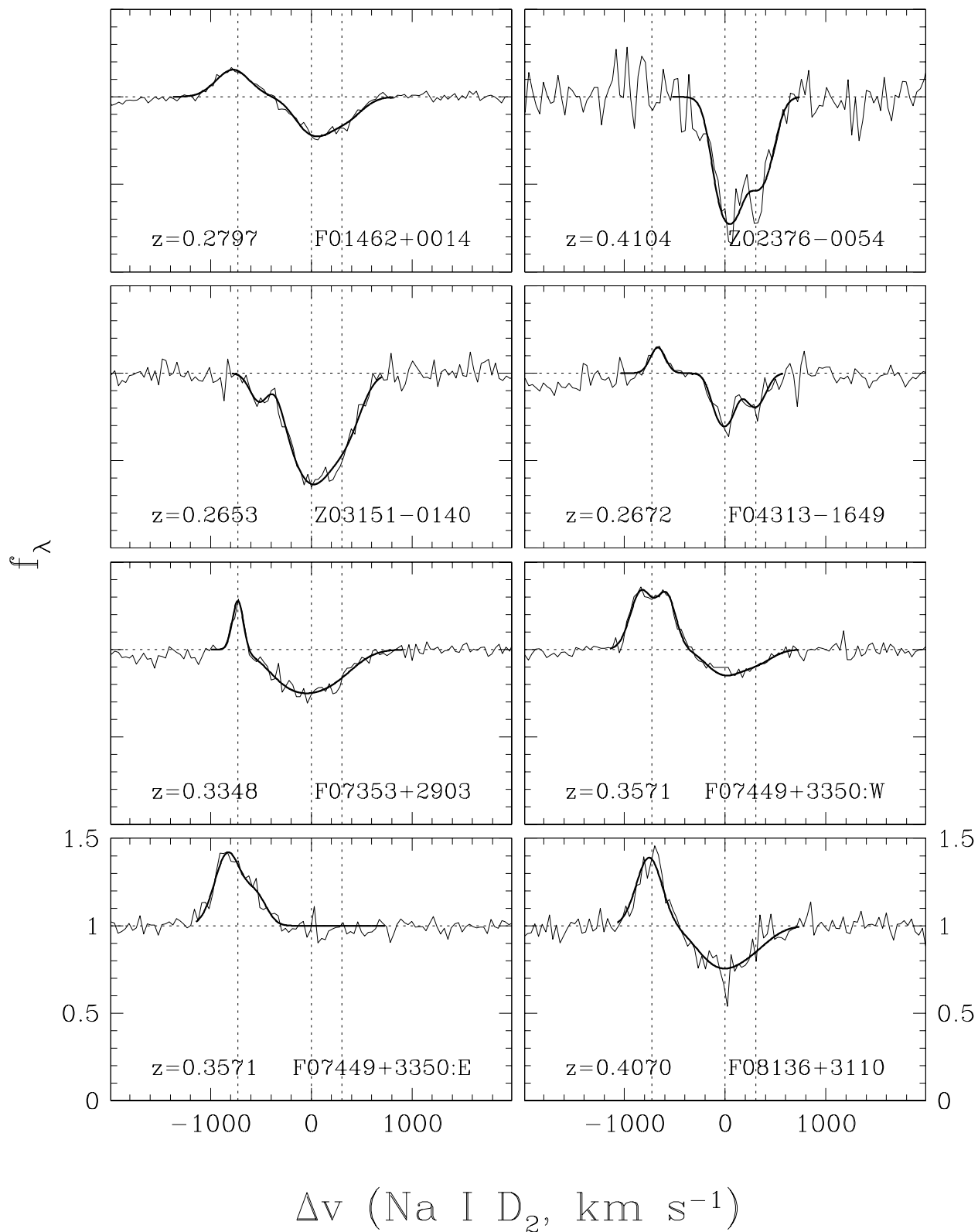


Fig. 4.— Spectra of the Na I D line in our $z > 0.25$ ULIRG subsample. See Figure 2 for more details.

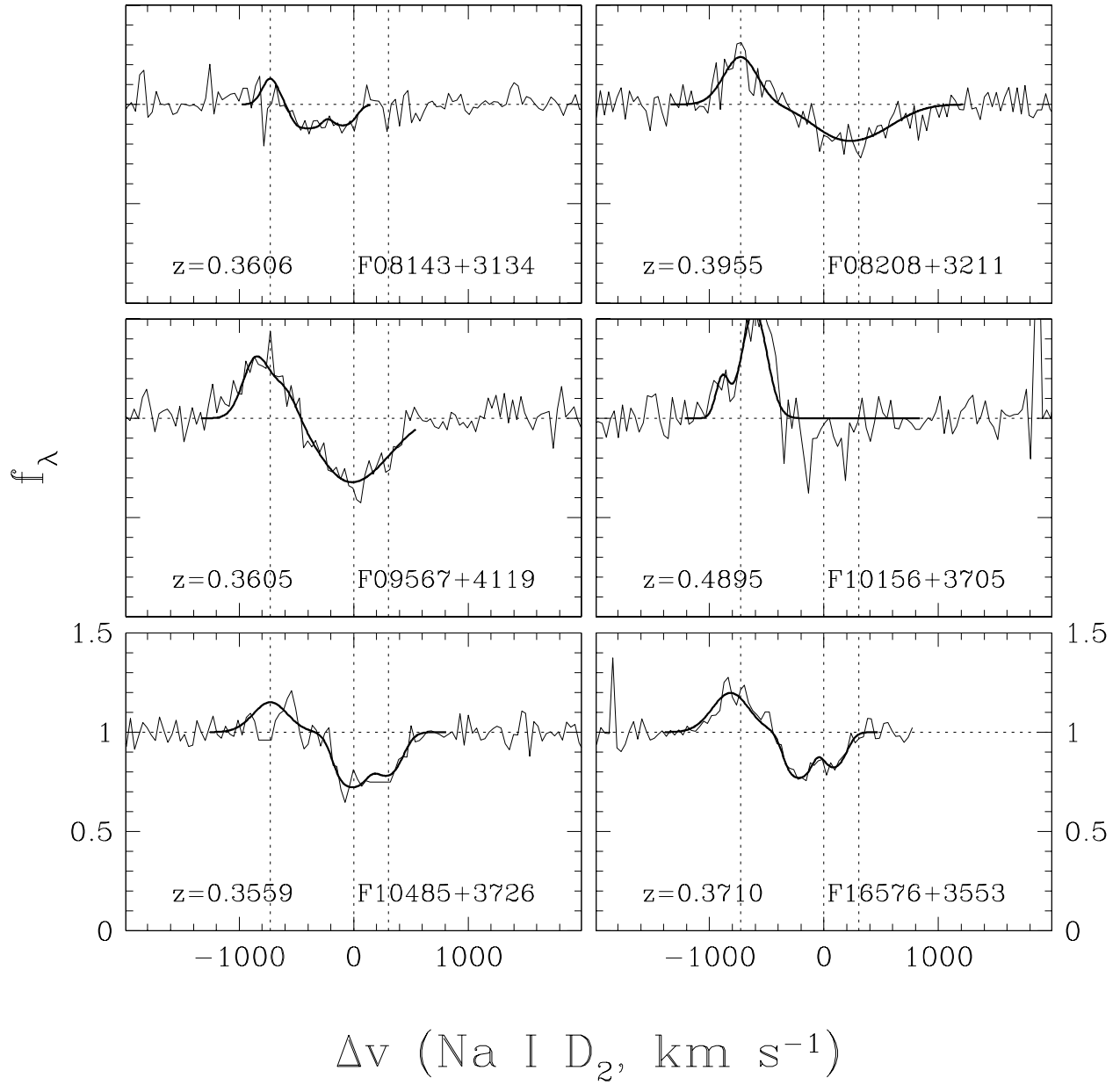


Fig. 4.— *Continued.*

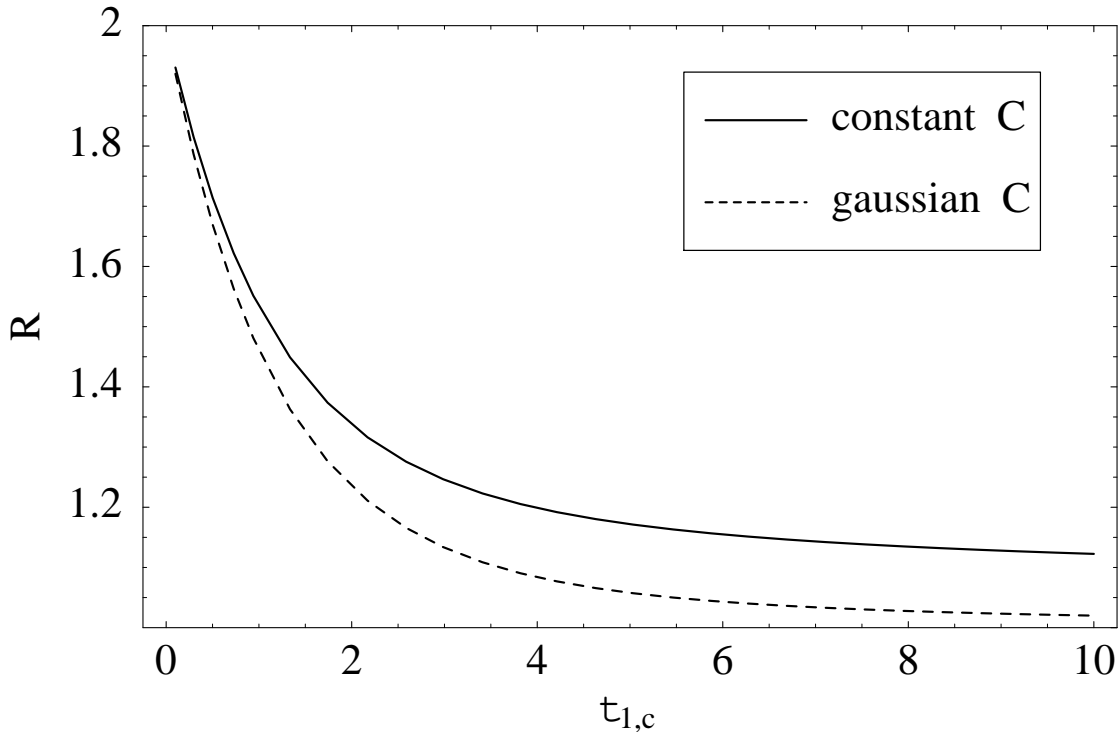


Fig. 5.— Equivalent width ratio of the Na I D doublet, $R \equiv W_{eq}(D_2)/W_{eq}(D_1)$, as a function of the central optical depth of the red line, $\tau_{1,c}$. We assume a Maxwellian velocity distribution and either (a) a constant covering fraction C_f (solid line) or (b) a Gaussian $C_f(\lambda)$ with the same width as the velocity distribution (dashed line). If the equivalent widths are measured by fitting Gaussian intensity profiles and the doublet ratio R yields a high optical depth, there is a contradiction. The intensity profile should not be Gaussian for a high optical depth if the velocity profile is Maxwellian and C_f is constant, as assumed in the doublet ratio method. One way to produce Gaussian profiles is if the covering fraction varies with velocity, which is not allowed in the doublet ratio method. If the doublet ratio method is applied in this case, τ is severely overestimated for $R \lesssim 1.2$. See §5.3 for more details.

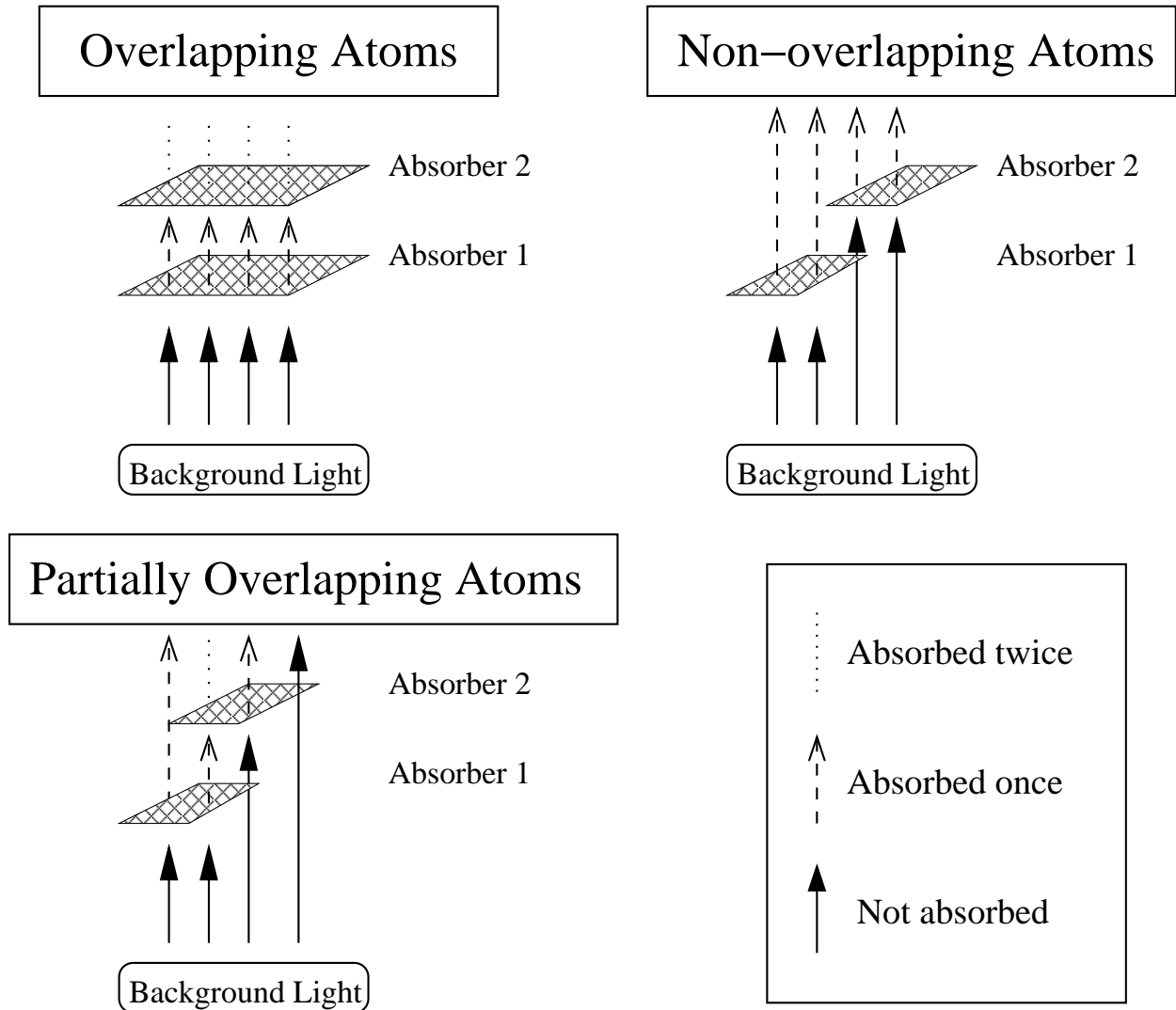


Fig. 6.— Possible geometries of absorbers along the line of sight. The possibilities are (1) absorbers that completely overlap, (2) absorbers that have no overlap, and (3) absorbers that overlap partially, such that the covering fraction describes both the fractional coverage of both the background light and the other absorber. In our analysis, we use case (1) to group the doublet lines in a single velocity component, and case (3) to group different velocity components in a single galaxy. See §5.4 for further discussion.

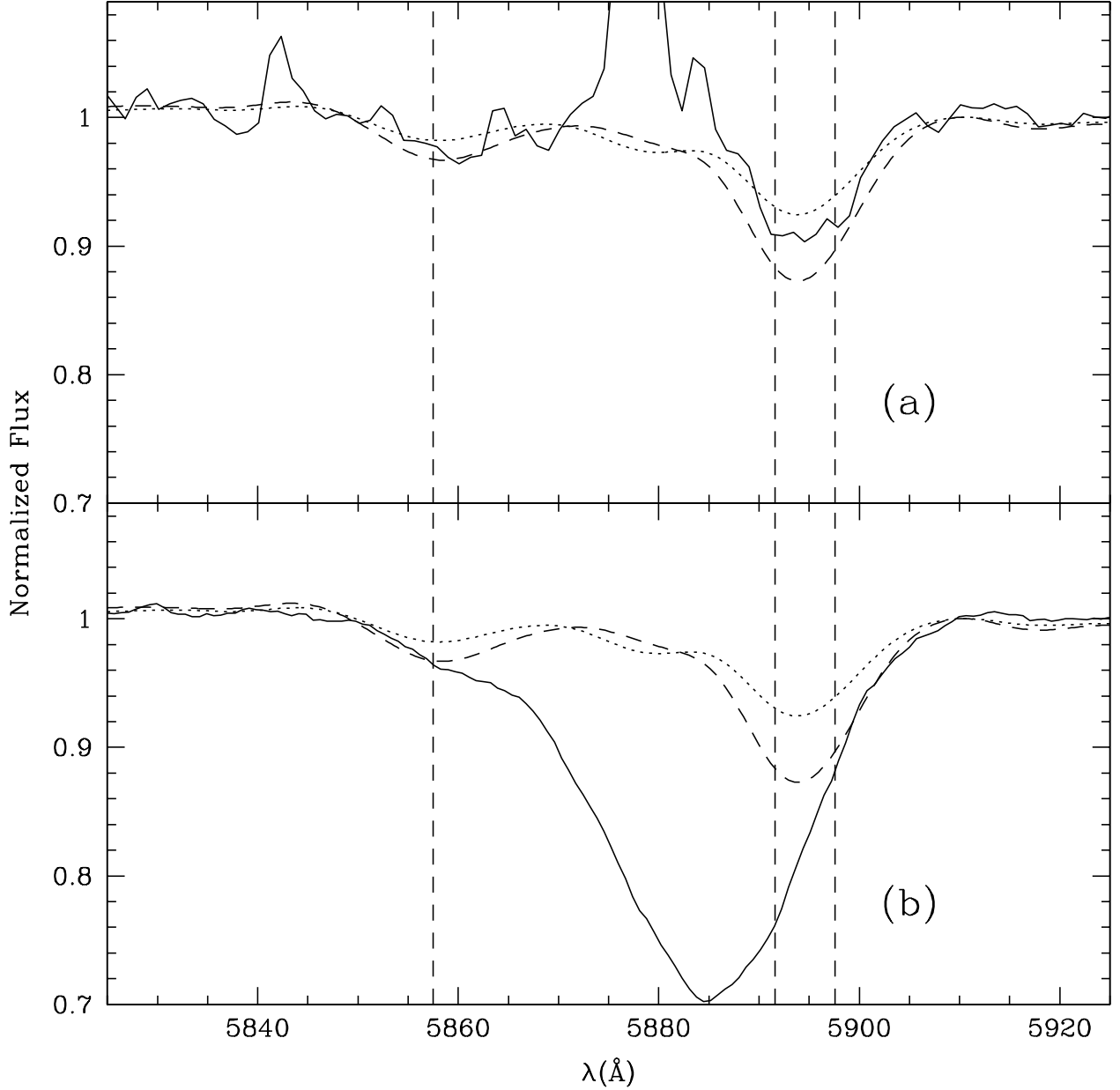


Fig. 7.— Spectra of two galaxies, (a) F15549+4201 and (b) F10378+1108, in the region of Na I D, boxcar smoothed by $\sim 150 \text{ km s}^{-1}$ to bring out weak stellar features. The dotted and dashed lines show stellar population mixes at solar metallicity from the models of González Delgado et al. (2005). The dotted line shows a mix of a 10% 40 Myr stellar population and a 90% 10 Gyr stellar population, where the percentages represent stellar mass fractions. The dashed line shows a 1% 40 Myr, 99% 10 Gyr mix. We convolve the models with a $\sigma = 200 \text{ km s}^{-1}$ Gaussian. The models are normalized to unity at 5910 \AA , and we add a linear normalization of $-6 \times 10^{-4} \text{ \AA}^{-1}$ to match the data. The strong stellar feature blueward of Na I D and the rest-frame wavelengths of Na I D are marked with a vertical dashed line. The stellar models fit the absorption lines of F15549+4201 well, consistent with the fact that it does not possess a wind. However, the strong, blueshifted interstellar component of F10378+1108 is obvious. The blue stellar feature in this galaxy has little impact on the interstellar line profile. See §6.3 for further discussion.

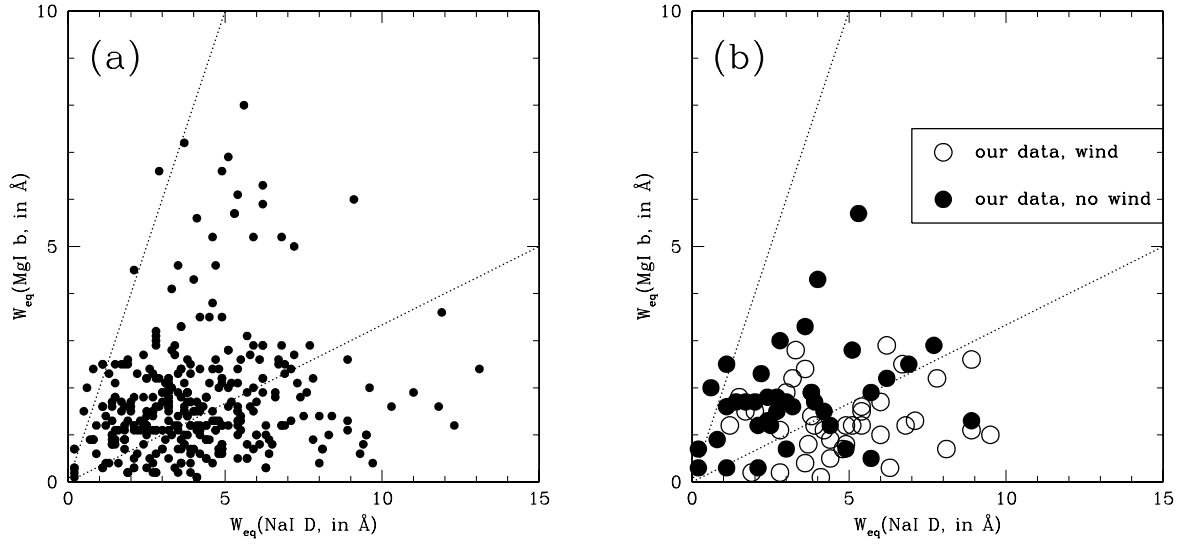


Fig. 8.— Equivalent width of Mg I b vs. equivalent width of Na I D for (a) a large number of nearby galaxies and (b) our sample. The upper line is calculated using the assumption $W_{eq}^*(\text{Na I D}) = 0.5 \times W_{eq}(\text{Mg I } b)$, and is a by-eye estimate to the upper envelope. Deviations from this line are due to the presence of interstellar absorption in the Na I D line. The interstellar contribution is typically dominant in infrared-luminous galaxies. The lower line is a line below which most galaxies have winds, and above which most galaxies do *not* have winds. This detection rate threshold is independent of SFR. Note that these plots include both starbursts (from this work) and AGN (Rupke, Veilleux, & Sanders 2005b). See §6.3.3 for further discussion.

Table 1. Subsample Average Properties

Quantity (1)	IRGs (2)	low- z ULIRGs (3)	high- z ULIRGs (4)
N_{gals}	35	30	13
z	$0.031^{+0.04}_{-0.02}$	$0.129^{+0.07}_{-0.04}$	$0.360^{+0.07}_{-0.06}$
$\log[L_{IR}/L_{\odot}]$	11.36 ± 0.4	12.21 ± 0.2	12.45 ± 0.2
SFR ($M_{\odot} \text{ yr}^{-1}$)	40^{+55}_{-23}	225^{+95}_{-67}	389^{+212}_{-137}

Note. — For each quantity, we list the median and 1σ dispersions, under the assumption of a Gaussian distribution in the log of the quantity.

Table 2. Galaxy Properties

Name (1)	Other (2)	z (3)	Type (4)	L_{IR} (5)	R (6)	$K^{(l)}$ (7)	SFR (8)	v_c (9)	W_{eq} (10)	Run (11)	t_{exp} (12)	PA (13)	Refs (14)
IRGs													
F00521+2858	UGC.556	0.0155	L	10.84	-24.29	-24.29	12	204	2.47	8	3600	90	34
Z01092-0139	...	0.1533	H	11.65	...	-24.99	77	...	2.71	13	7200	160	2
F01250-0848	Mrk.995	0.0488	H	11.68	...	-25.85	83	418	4.20	13	2700	40	5
F01417+1651:N	III.Zw.35	0.0276	L	11.56	-24.23	-24.23	63	...	2.01	13	4500	15	34ab
F01417+1651:S	...	0.0271	H	1.57	34ab
F01484+2220	NGC.695	0.0323	H	11.64	...	-25.99	75	416	3.67	13	1800	55	34
F02114+0456:SW	IC.214	0.0296	H	11.42	45	390	1.70	13	2700	55	34
F02433+1544	...	0.0254	H	10.99	...	-24.43	17	187	5.81	13	2700	140	4
F02437+2122	...	0.0234	L	11.10	...	-25.02	22	76	6.42	8	1800	55	34
F02509+1248	NGC.1134	0.0122	...	10.85	-25.26	-25.26	12	248	4.12	8	2400	148	3ab
F02512+1446:S	UGC.2369	0.0315	H	11.63	74	...	3.15	13	4500	0	34
Z03009-0213	...	0.1191	H	11.36	...	-25.10	40	269	2.41	9	5400	0	2
F1_5	...	0.4786	H	11.85	122	...	5.18	4	7200	0	6
F03359+1523	...	0.0357	H	11.48	-20.06	-24.17	52	...	0.60	13	2700	70	34a
F03514+1546	CGCG.465-012	0.0222	H	11.15	-21.38	-24.82	24	270	4.31	8	3600	55	34b
F04097+0525	UGC.2982	0.0179	H	11.13	...	-25.11	23	229	2.80	8	4800	55	34
F04315-0840	NGC.1614	0.0159	H	11.60	-25.20	-25.20	69	...	5.76	8	900	30	34b
F04326+1904	UGC.3094	0.0247	...	11.44	...	-25.58	48	268	4.57	8	3600	180	3
F05187-1017	...	0.0285	L	11.23	...	-24.30	29	207	3.88	13	2700	100	34
F08354+2555	NGC.2623	0.0182	L	11.55	-24.45	-24.45	61	...	2.65	8	4800	180	34
F08498+3513	...	0.1895	L	11.75	-25.70	-25.70	97	328	2.45	9	7200	0	2
F09120+4107	NGC.2785	0.0085	H	10.70	...	-23.88	9	169	3.80	8	3600	120	34
F09320+6134	UGC.5101	0.0395	L	11.96	...	-25.92	157	268	3.55	15	10800	90	34
F10015-0614	NGC.3110	0.0166	H	11.31	-25.24	-25.24	35	203	3.36	8	2400	170	34
F13532+2517	CGCG.132-048	0.0293	L	10.99	...	-24.26	17	161	9.07	11	2400	20	-
F13565+3519	MCG+06-31-036	0.0347	H	11.33	...	-25.25	37	266	3.10	11	2400	130	-

Table 2—Continued

Name (1)	Other (2)	z (3)	Type (4)	L_{IR} (5)	R (6)	$K^{(l)}$ (7)	SFR (8)	v_c (9)	W_{eq} (10)	Run (11)	t_{exp} (12)	PA (13)	Refs (14)
F15364+3320	CGCG.194-012	0.0222	H	10.21	...	-23.42	3	...	1.33	11	2400	90	4
F15386+3807	...	0.1828	H	11.62	...	-25.61	72	...	5.99	12	7200	270	2
F15549+4201	UGC.10099	0.0348	H	11.10	...	-24.79	22	255	1.05	11	3600	130	4
F16130+2725	...	0.0459	H	10.68	8	...	1.20	13	4800	60	4
F16504+0228	NGC.6240	0.0243	L	11.86	-22.96	-26.40	125	458	6.75	15	7200	90	34
F21484-1314	...	0.0768	H	11.50	...	-25.48	55	...	3.61	13	3600	100	1
F21549-1206	...	0.0511	L	11.19	-24.90	-24.90	27	187	2.46	13	4800	125	4
F22213-0238	...	0.0566	H	11.33	...	-24.86	37	180	3.37	13	3600	110	4
F22220-0825	...	0.0604	H	11.40	...	-24.73	44	...	4.54	13	4800	35	4
F22338-1015	...	0.0623	H	11.36	...	-24.99	40	...	3.34	13	4800	25	4
low-z ULIRGs													
F00188-0856	...	0.1283	L	12.38	-21.81	-24.90	333	...	4.26	3	5400	0	1
F01298-0744	...	0.1361	H	12.35	-21.18	-23.70	308	...	4.82	10	1800	15	1
F02411+0353:SW	...	0.1434	H	12.24	-25.35	-25.35	240	...	2.17	3	5400	25	1
F02411+0353:NE	...	0.1441	H	3.32	1
F03250+1606	...	0.1290	L	12.13	-21.98	-24.91	185	...	6.90	2	1800	0	1
F08231+3052	...	0.2478	L	12.32	...	-25.96	288	...	6.92	9	5400	0	2
F08474+1813	...	0.1454	L	12.22	-20.44	-23.30	230	...	1.99	10	900	130	1
F08591+5248	...	0.1574	...	12.24	-21.83	-25.05	241	...	5.15	3	3600	80	1
F09039+0503	...	0.1252	L	12.10	-21.35	-24.75	173	...	3.33	2	1800	0	1
F09116+0334	...	0.1454	L	12.18	-22.11	-26.16	211	...	3.97	1	1200	0	1
F09539+0857	...	0.1290	L	12.13	-20.54	-23.56	187	...	5.05	2	1800	0	1
F10091+4704	...	0.2451	L	12.64	-22.31	-25.38	597	...	3.42	9	5400	0	1
F10190+1322:W	...	0.0766	H	12.00	-25.45	-25.45	139	180	5.67	2	900	0	1
F10190+1322:E	...	0.0759	L	239	8.85	1
F10378+1108	...	0.1363	L	12.32	-22.15	-24.66	291	...	7.08	2	1800	0	1
F10494+4424	...	0.0919	L	12.17	-21.23	-24.38	203	...	4.05	8	5400	10	1

Table 2—Continued

Name (1)	Other (2)	z (3)	Type (4)	L_{IR} (5)	R (6)	$K^{(\prime)}$ (7)	SFR (8)	v_c (9)	W_{eq} (10)	Run (11)	t_{exp} (12)	PA (13)	Refs (14)
F10565+2448	...	0.0430	H	12.04	-22.31	-25.58	151	177	8.37	8	2700	53	34b
F11028+3130	...	0.1986	L	12.43	-21.03	-24.13	368	...	2.43	9	6300	0	1
F11387+4116	...	0.1489	H	12.20	-21.52	-24.66	219	...	7.85	2	1800	0	1
F11506+1331	...	0.1274	H	12.33	-21.41	-24.37	297	...	2.66	12	7200	43	1
F11582+3020	...	0.2234	L	12.60	-21.53	-24.88	544	...	2.85	9	7200	0	1
F14060+2919	...	0.1169	H	12.10	-21.98	-25.21	173	...	1.99	11	5400	48	1
F14197+0813	...	0.1305	L	12.16	-22.21	-24.60	197	...	1.70	12	7200	124	1
F15206+3342	...	0.1254	H	12.20	-21.99	-24.82	218	...	2.13	11	5400	80	1
F16333+4630:W	...	0.1908	L	12.43	-25.42	-25.42	367	...	4.24	12	3600	74	1
F16333+4630:E	...	0.1908	H	1.81	1
F16474+3430:S	...	0.1121	H	12.18	-25.34	-25.34	211	...	2.47	11	7200	164	1
F16474+3430:N	...	0.1126	H	2.62	1
F16487+5447:W	...	0.1038	L	12.15	-24.69	-24.69	194	...	0.95	11,13	9000	68	1
F16487+5447:E	...	0.1038	L	3.51	1
F17068+4027	...	0.1794	H	12.38	-21.47	-24.80	334	...	2.28	12	3600	0	1
F17207-0014	...	0.0428	L	12.35	...	-25.60	306	324	6.14	11	2400	96	3
I20046-0623:W	...	0.0840	H	12.08	166	205	1.51	12	1800	70	-
I20046-0623:E	...	0.0847	H	1.45	-
F20414-1651	...	0.0872	H	12.32	-21.01	-23.91	290	...	2.54	11,13	6000	170	1
F23234+0946:W	...	0.1279	L	12.11	-25.25	-25.25	179	215	4.87	10	2100	113	1
F23234+0946:E	...	0.1277	L	160	4.01	1
high-z ULIRGs													
F01462+0014	...	0.2797	L	12.34	...	-25.86	302	...	2.67	10	3600	53	2
Z02376-0054	...	0.4104	L	12.64	...	-26.13	595	...	7.70	4	5400	0	2
Z03151-0140	...	0.2653	L	12.15	...	-26.12	195	...	8.86	10	1800	0	2
F04313-1649	...	0.2672	L	12.66	-22.01	-24.54	626	222	2.42	2	2400	0	1
F07353+2903	...	0.3348	L	12.36	...	-25.91	316	...	3.97	4,6	7200	0	2

Table 2—Continued

Name (1)	Other (2)	z (3)	Type (4)	L_{IR} (5)	R (6)	$K^{(\prime)}$ (7)	SFR (8)	v_c (9)	W_{eq} (10)	Run (11)	t_{exp} (12)	PA (13)	Refs (14)
F07449+3350:W	...	0.3571	L	12.75	...	-26.27	776	...	1.69	2,4,10	8400	127,0	2
F07449+3350:E	...	0.3571	L	0.00	2,10	6000	127	2
F08136+3110	...	0.4070	H	12.46	...	-26.30	398	...	3.20	4,6,10	9240	0	2
F08143+3134	...	0.3606	...	12.38	...	-25.99	329	...	1.16	10	3600	140	2
F08208+3211	...	0.3955	H	12.49	...	-25.83	426	...	2.76	4,10	7200	0	2
F09567+4119	...	0.3605	L	12.45	...	-26.49	389	...	4.39	10	1800	118	2
F10156+3705	...	0.4895	H	12.82	...	-26.08	908	...	0.00	4	3600	0	2
F10485+3726	...	0.3559	L	12.34	...	-25.26	303	...	2.95	4,10	6600	0	2
F16576+3553	...	0.3710	L	12.38	...	-24.97	331	...	2.03	5,6	7200	0	2

References. — (1) Kim & Sanders 1998; Veilleux et al. 1999a; (2) Stanford et al. 2000; (3) Sanders et al. 2003; (4) Kim et al. 1995; Veilleux et al. 1995; (5) Kewley et al. 2001; (6) Clements et al. 2001; (a) Lehnert & Heckman 1995, 1996; (b) Heckman et al. 2000.

Note. — Col.(1): *IRAS* Faint Source Catalog label, plus nuclear ID (e.g., N = north). Only 1 object is not found in the FSC. Col.(2): Another name. Col.(3): Heliocentric redshift (§3.4). Col.(4): Optical spectral type (§§2 and 3.3). Col.(5): Infrared luminosity (8 – 1000 μm), in logarithmic units of L_{\odot} . Col.(6): K - or K' -band absolute magnitude (§2.4; Stanford et al. 2000; Veilleux et al. 2002; Jarrett et al. 2003; 2MASS). 2MASS magnitudes are ‘total’ or within a 20 mag/ \square'' aperture. Col.(7): R-band absolute magnitude (§2.4; Armus et al. 1990; Lehnert & Heckman 1995; Veilleux et al. 2002). Col.(8): Star formation rate, computed from the infrared luminosity using a correction for AGN contribution to L_{IR} (§2). Col.(9): Circular velocity, given by $v_c^2 = 2\sigma^2 + v_{rot}^2$. (See §2.4 for references). Col.(10): Rest-frame equivalent width of Na I D, in \AA , as computed from our model fits (§5). Col.(11): Observing run (see Table 3). Col.(12): Total exposure time in seconds. Col.(13): Slit position angle. Col.(14): Reference. Numbered references are infrared survey references; lettered references are previous superwind surveys.

Table 3. Observing Runs

Run (1)	UT Dates (2)	Telescope/Instrument (3)	CCD (4)	Seeing (5)
1	2001 Jan 23-24	Keck II / ESI	MITLL	0'8–1'1
2	2001 Feb 27-28	Keck II / ESI	MITLL	0'6–1'1
3	2001 Oct 07-09	KPNO 4m / R-C Spec.	T2KB	1'4–1'6
4	2002 Jan 16-17	Keck II / ESI	MITLL	0'8–1'5
5	2002 Feb 16	Keck II / ESI	MITLL	1'2–1'5
6	2002 Mar 15	Keck II / ESI	MITLL	0'8
7	2002 Jul 10-13	KPNO 4m / R-C Spec.	T2KB	1'3
8	2002 Dec 27-30	KPNO 4m / R-C Spec.	T2KB	1'4–3'0
9	2002 Dec 31- 2003 Jan 01	MMT / Red Chan. Spec.	UA/ITL	1'4–2'0
10	2003 Jan 06	Keck II / ESI	MITLL	0'7
11	2003 May 30- 2003 Jun 02	KPNO 4m / R-C Spec.	T2KB	0'9–1'5
12	2003 Jun 03-04	MMT / Red Chan. Spec.	UA/ITL	1'0–1'5
13	2003 Sep 24-29	KPNO 4m / R-C Spec.	T2KB	0'7–1'0
14	2004 Apr 12-16	KPNO 4m / R-C Spec.	T2KB	0'9–1'6

Table 4. Outflow Component Properties

Name (1)	$\lambda_{1,c}$ (2)	Δv (3)	b (4)	$\tau_{1,c}$ (5)	C_f (6)	$N(\text{Na I})$ (7)	$N(\text{H})$ (8)
IRGs							
F00521+2858	5989.36	26 (± 2)	67 (± 8)	2.36 ($^{+0.63}_{-0.34}$)	0.38 ($^{+0.10}_{-0.06}$)	13.75	21.20
Z01092–0139	6798.96	-119 (± 18)	172 (± 59)	0.56 ($^{+\infty}_{-0.14}$)	0.38 ($^{+0.49}_{-0.10}$)	>13.53	>20.83
F01250–0848	6182.55	-107 (± 4)	233 (± 21)	0.83 ($^{+0.12}_{-0.12}$)	0.36 ($^{+0.05}_{-0.05}$)	13.83	21.13
F01417+1651:N	6061.11	87 (± 1)	75 (± 4)	1.03 ($^{+0.08}_{-0.07}$)	0.41 ($^{+0.03}_{-0.03}$)	13.44	20.90
F01417+1651:S	6058.93	74 (± 21)	226 (± 68)	0.07 ($^{+0.09}_{-0.01}$)	1.00 ($^{+0.00}_{-0.00}$)	12.75	20.21
F01484+2220	6086.31	-139 (± 3)	145 (± 9)	0.94 ($^{+0.10}_{-0.09}$)	0.43 ($^{+0.05}_{-0.04}$)	13.69	20.98
F02114+0456:SW	6072.63	11 (± 6)	136 (± 17)	0.65 ($^{+0.17}_{-0.12}$)	0.26 ($^{+0.07}_{-0.05}$)	13.50	20.80
F02433+1544	6045.41	-97 (± 12)	192 (± 43)	1.66 ($^{+\infty}_{-0.56}$)	0.28 ($^{+0.34}_{-0.09}$)	>14.06	>21.47
...	6046.84	-26 (± 4)	84 (± 18)	0.72 ($^{+0.30}_{-0.10}$)	0.61 ($^{+0.25}_{-0.09}$)	13.33	20.75
F02437+2122	6030.17	-240 (± 9)	82 (± 27)	1.26 ($^{+1.93}_{-0.47}$)	0.27 ($^{+0.41}_{-0.10}$)	13.57	20.87
...	6035.94	46 (± 3)	100 (± 13)	2.34 ($^{+0.59}_{-0.33}$)	0.54 ($^{+0.14}_{-0.08}$)	13.92	21.22
F02509+1248	5969.77	27 (± 9)	227 (± 36)	0.22 ($^{+0.09}_{-0.06}$)	0.77 ($^{+0.16}_{-0.11}$)	13.24	20.54
...	5970.04	41 (± 5)	65 (± 38)	0.72 ($^{+0.42}_{-0.14}$)	0.30 ($^{+0.18}_{-0.06}$)	13.22	20.51
F02512+1446:S	6074.37	-406 (± 4)	85 (± 19)	0.24 ($^{+0.14}_{-0.02}$)	0.48 ($^{+0.29}_{-0.05}$)	12.86	20.15
...	6080.78	-90 (± 7)	168 (± 28)	0.77 ($^{+0.21}_{-0.15}$)	0.27 ($^{+0.08}_{-0.05}$)	13.66	20.96
Z03009–0213	6601.33	62 (± 6)	183 (± 22)	0.60 ($^{+0.14}_{-0.11}$)	0.31 ($^{+0.07}_{-0.06}$)	13.59	20.89
F1.5	8709.25	-374 (± 5)	122 (± 16)	0.31 ($^{+0.10}_{-0.03}$)	0.76 ($^{+0.23}_{-0.08}$)	13.14	20.43
...	8717.86	-78 (± 14)	198 (± 52)	0.56 ($^{+0.19}_{-0.09}$)	0.37 ($^{+0.13}_{-0.06}$)	13.60	20.89
F03359+1523	6108.41	1 (± 25)	159 (± 58)	0.21 ($^{+\infty}_{-0.06}$)	0.20 ($^{+0.66}_{-0.03}$)	>13.07	>20.54
F03514+1546	6026.55	-103 (± 3)	188 (± 13)	0.60 ($^{+0.08}_{-0.07}$)	0.54 ($^{+0.07}_{-0.06}$)	13.60	20.94
F04097+0525	6003.31	15 (± 2)	70 (± 7)	1.52 ($^{+0.25}_{-0.18}$)	0.50 ($^{+0.08}_{-0.06}$)	13.58	20.87
F04315–0840	5989.48	-104 (± 5)	154 (± 12)	1.37 ($^{+0.14}_{-0.13}$)	0.47 ($^{+0.05}_{-0.05}$)	13.88	21.17
...	5993.50	98 (± 4)	48 (± 10)	3.24 ($^{+4.03}_{-1.28}$)	0.16 ($^{+0.20}_{-0.06}$)	13.74	21.04
F04326+1904	6044.87	80 (± 15)	252 (± 52)	0.22 ($^{+0.20}_{-0.05}$)	0.93 ($^{+0.05}_{-0.01}$)	13.30	20.59
F05187–1017	6065.92	14 (± 2)	74 (± 7)	2.32 ($^{+0.45}_{-0.29}$)	0.54 ($^{+0.10}_{-0.07}$)	13.79	21.23
F08354+2555	6003.41	-164 (± 14)	286 (± 49)	0.08 ($^{+0.06}_{-0.02}$)	1.00 ($^{+0.00}_{-0.00}$)	12.89	20.31
...	6005.12	-79 (± 6)	56 (± 33)	2.17 ($^{+1.55}_{-0.78}$)	0.11 ($^{+0.08}_{-0.04}$)	13.64	21.05
F08498+3513	7015.80	28 (± 9)	180 (± 32)	0.95 ($^{+0.41}_{-0.25}$)	0.24 ($^{+0.10}_{-0.06}$)	13.78	21.08
F09120+4107	5948.10	12 (± 2)	74 (± 7)	1.82 ($^{+0.32}_{-0.21}$)	0.59 ($^{+0.11}_{-0.07}$)	13.68	21.21
F09320+6134	6130.18	-16 (± 2)	11 (± 10)	5.00 ($^{+0.33}_{-1.38}$)	0.12 ($^{+0.01}_{-0.03}$)	13.30	20.59
...	6130.73	11 (± 3)	194 (± 12)	0.57 ($^{+0.06}_{-0.06}$)	0.43 ($^{+0.04}_{-0.04}$)	13.59	20.89
F10015–0614	5993.01	-134 (± 7)	36 (± 32)	5.00 ($^{+\infty}_{-1.55}$)	0.11 ($^{+0.02}_{-0.03}$)	>13.80	>21.10
...	5994.56	-57 (± 7)	150 (± 22)	1.29 ($^{+0.35}_{-0.30}$)	0.29 ($^{+0.08}_{-0.07}$)	13.84	21.14
F13532+2517	6065.67	-238 (± 7)	321 (± 24)	0.94 ($^{+0.14}_{-0.14}$)	0.52 ($^{+0.08}_{-0.08}$)	14.03	21.49
...	6071.60	54 (± 3)	38 (± 15)	2.33 ($^{+1.24}_{-0.50}$)	0.30 ($^{+0.16}_{-0.06}$)	13.50	20.95

Table 4—Continued

Name (1)	$\lambda_{1,c}$ (2)	Δv (3)	b (4)	$\tau_{1,c}$ (5)	C_f (6)	$N(\text{Na I})$ (7)	$N(\text{H})$ (8)
F13565+3519	6102.13	24 (± 2)	95 (± 7)	0.51 ($^{+0.07}_{-0.04}$)	0.80 ($^{+0.11}_{-0.06}$)	13.24	20.54
F15364+3320	6027.39	-51 (± 7)	95 (± 21)	1.20 ($^{+1.02}_{-0.34}$)	0.20 ($^{+0.17}_{-0.06}$)	13.61	21.24
F15386+3807	6967.94	-331 (± 8)	123 (± 20)	2.58 ($^{+1.18}_{-0.49}$)	0.26 ($^{+0.12}_{-0.05}$)	14.05	21.35
...	6972.80	-122 (± 3)	97 (± 11)	2.62 ($^{+0.71}_{-0.42}$)	0.37 ($^{+0.10}_{-0.06}$)	13.96	21.25
F15549+4201	6103.24	-21 (± 8)	174 (± 26)	0.58 ($^{+0.20}_{-0.12}$)	0.14 ($^{+0.05}_{-0.03}$)	13.56	20.90
F16130+2725	6168.90	20 (± 12)	111 (± 29)	0.23 ($^{+0.21}_{-0.03}$)	0.52 ($^{+0.48}_{-0.06}$)	12.95	20.25
F16504+0228	6037.14	-99 (± 3)	59 (± 9)	5.00 ($^{+\infty}_{-1.02}$)	0.18 ($^{+0.01}_{-0.04}$)	>14.03	>21.32
...	6037.66	-74 (± 3)	292 (± 16)	0.27 ($^{+0.03}_{-0.02}$)	0.88 ($^{+0.10}_{-0.06}$)	13.45	20.75
F21484-1314	6352.18	69 (± 3)	92 (± 9)	1.57 ($^{+0.31}_{-0.23}$)	0.48 ($^{+0.09}_{-0.07}$)	13.71	21.01
F21549-1206	6199.08	11 (± 6)	138 (± 19)	1.20 ($^{+0.40}_{-0.25}$)	0.26 ($^{+0.09}_{-0.05}$)	13.77	21.09
F22213-0238	6231.88	11 (± 5)	132 (± 15)	1.05 ($^{+0.22}_{-0.17}$)	0.40 ($^{+0.09}_{-0.07}$)	13.69	21.02
F22220-0825	6247.30	-305 (± 37)	213 (± 83)	1.35 ($^{+1.15}_{-0.59}$)	0.23 ($^{+0.20}_{-0.10}$)	14.01	21.36
...	6252.63	-49 (± 10)	91 (± 24)	2.95 ($^{+1.55}_{-1.38}$)	0.17 ($^{+0.09}_{-0.08}$)	13.98	21.33
F22338-1015	6265.48	30 (± 7)	227 (± 26)	0.16 ($^{+0.04}_{-0.01}$)	1.00 ($^{+0.00}_{-0.00}$)	13.11	20.41
low-z ULIRGs							
F00188-0856	6650.32	-176 (± 12)	271 (± 57)	1.09 ($^{+0.60}_{-0.35}$)	0.28 ($^{+0.16}_{-0.09}$)	14.02	21.34
F01298-0744	6691.47	-392 (± 10)	264 (± 39)	0.19 ($^{+0.05}_{-0.01}$)	0.85 ($^{+0.11}_{-0.02}$)	13.26	20.83
...	6697.95	-101 (± 4)	99 (± 17)	0.12 ($^{+0.04}_{-0.01}$)	1.00 ($^{+0.00}_{-0.00}$)	12.63	20.20
F02411+0353:SW	6744.62	60 (± 26)	333 (± 104)	0.16 ($^{+0.46}_{-0.02}$)	0.46 ($^{+0.33}_{-0.02}$)	13.27	20.57
F02411+0353:NE	6743.34	-180 (± 8)	151 (± 25)	1.03 ($^{+0.36}_{-0.23}$)	0.36 ($^{+0.12}_{-0.08}$)	13.74	21.04
F03250+1606	6648.54	-442 (± 8)	197 (± 34)	7.22 ($^{+6.39}_{-2.89}$)	0.10 ($^{+0.09}_{-0.04}$)	14.71	22.02
...	6655.69	-120 (± 4)	280 (± 21)	0.57 ($^{+0.05}_{-0.09}$)	0.49 ($^{+0.05}_{-0.07}$)	13.76	21.07
F08231+3052	7360.30	54 (± 4)	191 (± 12)	0.47 ($^{+0.07}_{-0.03}$)	1.00 ($^{+0.00}_{-0.00}$)	13.51	20.80
F08474+1813	6755.09	1 (± 2)	97 (± 6)	0.46 ($^{+0.05}_{-0.04}$)	0.55 ($^{+0.06}_{-0.05}$)	13.20	20.85
F08591+5248	6822.55	-144 (± 11)	366 (± 49)	0.15 ($^{+0.08}_{-0.01}$)	1.00 ($^{+0.00}_{-0.00}$)	13.30	20.60
F09039+0503	6624.59	-513 (± 6)	83 (± 16)	4.24 ($^{+3.32}_{-1.51}$)	0.12 ($^{+0.10}_{-0.04}$)	14.10	21.45
...	6631.69	-192 (± 20)	224 (± 95)	0.12 ($^{+0.25}_{-0.01}$)	0.40 ($^{+0.43}_{-0.02}$)	12.97	20.32
...	6637.60	75 (± 12)	111 (± 35)	0.08 ($^{+0.04}_{-0.01}$)	1.00 ($^{+0.00}_{-0.00}$)	12.49	19.84
...	6640.13	190 (± 4)	35 (± 15)	0.72 ($^{+0.20}_{-0.11}$)	0.24 ($^{+0.07}_{-0.04}$)	12.95	20.30
F09116+0334	6752.32	-122 (± 2)	313 (± 14)	0.39 ($^{+0.03}_{-0.03}$)	0.43 ($^{+0.03}_{-0.03}$)	13.63	20.93
F09539+0857	6652.08	-282 (± 3)	283 (± 22)	0.38 ($^{+0.05}_{-0.04}$)	0.61 ($^{+0.09}_{-0.07}$)	13.58	21.18
F10091+4704	7339.99	-125 (± 6)	266 (± 26)	0.16 ($^{+0.05}_{-0.01}$)	0.85 ($^{+0.12}_{-0.03}$)	13.19	20.49
F10190+1322:W	6348.87	-21 (± 2)	188 (± 8)	0.79 ($^{+0.06}_{-0.06}$)	0.46 ($^{+0.04}_{-0.03}$)	13.72	21.02
...	6349.24	-3 (± 1)	55 (± 4)	1.32 ($^{+0.11}_{-0.09}$)	0.48 ($^{+0.04}_{-0.03}$)	13.41	20.71
F10190+1322:E	6346.41	58 (± 4)	196 (± 9)	0.98 ($^{+0.07}_{-0.07}$)	0.60 ($^{+0.04}_{-0.04}$)	13.84	21.13
...	6351.99	322 (± 1)	94 (± 5)	0.41 ($^{+0.05}_{-0.04}$)	1.00 ($^{+0.00}_{-0.00}$)	13.13	20.43

Table 4—Continued

Name	$\lambda_{1,c}$	Δv	b	$\tau_{1,c}$	C_f	$N(\text{Na I})$	$N(\text{H})$				
(1)	(2)	(3)	(4)	(5)	(6)	(7)	(8)				
F10378+1108	6689.05	-553	(± 7)	665	(± 39)	0.26	$\begin{smallmatrix} +0.05 \\ -0.03 \end{smallmatrix}$	0.42	$\begin{smallmatrix} +0.08 \\ -0.04 \end{smallmatrix}$	13.78	21.15
...	6689.46	-534	(± 5)	83	(± 17)	0.59	$\begin{smallmatrix} +0.18 \\ -0.11 \end{smallmatrix}$	0.16	$\begin{smallmatrix} +0.05 \\ -0.03 \end{smallmatrix}$	13.24	20.61
...	6695.96	-243	(± 9)	113	(± 12)	5.00	$\begin{smallmatrix} +\infty \\ -0.32 \end{smallmatrix}$	0.08	$\begin{smallmatrix} +0.01 \\ -0.01 \end{smallmatrix}$	>14.31	>21.67
F10494+4424	6433.40	-286	(± 12)	40	(± 36)	5.00	$\begin{smallmatrix} +\infty \\ -0.15 \end{smallmatrix}$	0.14	$\begin{smallmatrix} +0.06 \\ -0.00 \end{smallmatrix}$	>13.85	>21.28
...	6440.05	24	(± 7)	106	(± 22)	2.88	$\begin{smallmatrix} +\infty \\ -0.49 \end{smallmatrix}$	0.33	$\begin{smallmatrix} +0.18 \\ -0.06 \end{smallmatrix}$	>14.03	>21.46
F10565+2448	6144.99	-309	(± 13)	181	(± 19)	1.41	$\begin{smallmatrix} +0.24 \\ -0.17 \end{smallmatrix}$	0.49	$\begin{smallmatrix} +0.08 \\ -0.06 \end{smallmatrix}$	13.96	21.26
...	6148.43	-141	(± 5)	106	(± 13)	1.54	$\begin{smallmatrix} +0.53 \\ -0.42 \end{smallmatrix}$	0.43	$\begin{smallmatrix} +0.15 \\ -0.11 \end{smallmatrix}$	13.77	21.06
F11028+3130	7072.03	137	(± 8)	199	(± 35)	0.66	$\begin{smallmatrix} +0.23 \\ -0.16 \end{smallmatrix}$	0.27	$\begin{smallmatrix} +0.09 \\ -0.06 \end{smallmatrix}$	13.67	21.15
F11387+4116	6765.18	-466	(± 2)	112	(± 7)	0.19	$\begin{smallmatrix} +0.03 \\ -0.01 \end{smallmatrix}$	1.00	$\begin{smallmatrix} +0.00 \\ -0.00 \end{smallmatrix}$	12.87	20.24
...	6772.13	-158	(± 2)	196	(± 6)	0.75	$\begin{smallmatrix} +0.03 \\ -0.02 \end{smallmatrix}$	0.67	$\begin{smallmatrix} +0.03 \\ -0.02 \end{smallmatrix}$	13.72	21.09
F11506+1331	6647.26	-74	(± 4)	108	(± 14)	1.99	$\begin{smallmatrix} +0.59 \\ -0.36 \end{smallmatrix}$	0.28	$\begin{smallmatrix} +0.08 \\ -0.05 \end{smallmatrix}$	13.89	21.32
F11582+3020	7213.24	-76	(± 8)	195	(± 32)	0.85	$\begin{smallmatrix} +0.27 \\ -0.19 \end{smallmatrix}$	0.28	$\begin{smallmatrix} +0.09 \\ -0.06 \end{smallmatrix}$	13.77	21.10
F14060+2919	6583.86	-142	(± 7)	113	(± 28)	4.47	$\begin{smallmatrix} +\infty \\ -1.51 \end{smallmatrix}$	0.16	$\begin{smallmatrix} +0.69 \\ -0.05 \end{smallmatrix}$	>14.25	>21.55
F14197+0813	6663.68	-158	(± 8)	354	(± 37)	0.06	$\begin{smallmatrix} +0.02 \\ -0.00 \end{smallmatrix}$	0.84	$\begin{smallmatrix} +0.14 \\ -0.02 \end{smallmatrix}$	12.86	20.24
F15206+3342	6632.17	-213	(± 26)	244	(± 43)	1.19	$\begin{smallmatrix} +0.62 \\ -0.37 \end{smallmatrix}$	0.15	$\begin{smallmatrix} +0.08 \\ -0.05 \end{smallmatrix}$	14.01	21.35
F16333+4630:W	7022.00	-35	(± 11)	311	(± 35)	0.34	$\begin{smallmatrix} +0.10 \\ -0.05 \end{smallmatrix}$	0.34	$\begin{smallmatrix} +0.10 \\ -0.05 \end{smallmatrix}$	13.57	20.87
...	7024.49	71	(± 3)	103	(± 10)	0.29	$\begin{smallmatrix} +0.04 \\ -0.02 \end{smallmatrix}$	0.63	$\begin{smallmatrix} +0.09 \\ -0.05 \end{smallmatrix}$	13.02	20.32
F16333+4630:E	7019.62	-136	(± 17)	240	(± 74)	0.12	$\begin{smallmatrix} +0.17 \\ -0.02 \end{smallmatrix}$	0.64	$\begin{smallmatrix} +0.22 \\ -0.03 \end{smallmatrix}$	13.03	20.32
F16474+3430:S	6556.65	-101	(± 6)	200	(± 27)	1.01	$\begin{smallmatrix} +0.26 \\ -0.20 \end{smallmatrix}$	0.22	$\begin{smallmatrix} +0.06 \\ -0.04 \end{smallmatrix}$	13.86	21.15
F16474+3430:N	6558.10	-158	(± 16)	103	(± 23)	5.00	$\begin{smallmatrix} +\infty \\ -1.56 \end{smallmatrix}$	0.14	$\begin{smallmatrix} +0.02 \\ -0.04 \end{smallmatrix}$	>14.27	>21.56
...	6562.81	57	(± 40)	189	(± 56)	0.12	$\begin{smallmatrix} +\infty \\ -0.04 \end{smallmatrix}$	0.49	$\begin{smallmatrix} +0.29 \\ -0.01 \end{smallmatrix}$	>12.92	>20.22
F16487+5447:W	6508.07	-76	(± 20)	160	(± 40)	1.75	$\begin{smallmatrix} +\infty \\ -0.81 \end{smallmatrix}$	0.08	$\begin{smallmatrix} +0.09 \\ -0.04 \end{smallmatrix}$	>14.00	>21.36
F16487+5447:E	6509.55	-8	(± 16)	408	(± 69)	0.09	$\begin{smallmatrix} +0.07 \\ -0.01 \end{smallmatrix}$	1.00	$\begin{smallmatrix} +0.00 \\ -0.00 \end{smallmatrix}$	13.11	20.47
F17068+4027	6956.41	36	(± 10)	265	(± 56)	0.43	$\begin{smallmatrix} +0.25 \\ -0.10 \end{smallmatrix}$	0.27	$\begin{smallmatrix} +0.16 \\ -0.06 \end{smallmatrix}$	13.61	20.95
F17207–0014	6143.74	-298	(± 21)	177	(± 37)	2.16	$\begin{smallmatrix} +\infty \\ -0.87 \end{smallmatrix}$	0.35	$\begin{smallmatrix} +0.46 \\ -0.14 \end{smallmatrix}$	>14.13	>21.43
...	6150.41	27	(± 13)	85	(± 54)	1.83	$\begin{smallmatrix} +\infty \\ -0.69 \end{smallmatrix}$	0.20	$\begin{smallmatrix} +0.54 \\ -0.08 \end{smallmatrix}$	>13.74	>21.04
I20046–0623:W	6388.88	-191	(± 5)	37	(± 10)	5.00	$\begin{smallmatrix} +\infty \\ -2.76 \end{smallmatrix}$	0.10	$\begin{smallmatrix} +0.02 \\ -0.05 \end{smallmatrix}$	>13.82	>21.11
...	6393.67	33	(± 25)	285	(± 92)	0.06	$\begin{smallmatrix} +0.09 \\ -0.01 \end{smallmatrix}$	0.62	$\begin{smallmatrix} +0.21 \\ -0.02 \end{smallmatrix}$	12.80	20.10
I20046–0623:E	6398.11	48	(± 5)	197	(± 16)	0.09	$\begin{smallmatrix} +0.45 \\ -0.15 \end{smallmatrix}$	0.87	$\begin{smallmatrix} +0.07 \\ -0.02 \end{smallmatrix}$	12.78	20.08
F20414–1651	6408.99	-119	(± 11)	133	(± 34)	1.00	$\begin{smallmatrix} +0.75 \\ -0.30 \end{smallmatrix}$	0.31	$\begin{smallmatrix} +0.23 \\ -0.09 \end{smallmatrix}$	13.67	21.20
F23234+0946:W	6646.53	-240	(± 3)	235	(± 15)	0.33	$\begin{smallmatrix} +0.03 \\ -0.02 \end{smallmatrix}$	0.77	$\begin{smallmatrix} +0.08 \\ -0.06 \end{smallmatrix}$	13.44	20.73
F23234+0946:E	6653.00	97	(± 4)	159	(± 15)	1.13	$\begin{smallmatrix} +0.20 \\ -0.16 \end{smallmatrix}$	0.40	$\begin{smallmatrix} +0.07 \\ -0.06 \end{smallmatrix}$	13.81	21.11
high-z ULIRGs											
F01462+0014	7547.80	27	(± 3)	223	(± 13)	0.35	$\begin{smallmatrix} +0.03 \\ -0.03 \end{smallmatrix}$	0.42	$\begin{smallmatrix} +0.04 \\ -0.04 \end{smallmatrix}$	13.44	20.74
Z02376–0054	8319.04	41	(± 2)	159	(± 7)	0.87	$\begin{smallmatrix} +0.07 \\ -0.06 \end{smallmatrix}$	0.88	$\begin{smallmatrix} +0.07 \\ -0.06 \end{smallmatrix}$	13.69	20.99
Z03151–0140	7449.29	-518	(± 7)	120	(± 19)	0.09	$\begin{smallmatrix} +0.09 \\ -0.01 \end{smallmatrix}$	1.00	$\begin{smallmatrix} +0.00 \\ -0.00 \end{smallmatrix}$	12.57	19.86

Table 4—Continued

Name	$\lambda_{1,c}$	Δv	b		$\tau_{1,c}$		C_f	$N(\text{Na I})$		$N(\text{H})$	
(1)	(2)	(3)	(4)	(5)	(6)	(7)	(8)	(9)	(10)		
...	7462.07	-4	(± 3)	221	(± 11)	0.59	($^{+0.04}_{-0.04}$)	0.87	($^{+0.07}_{-0.06}$)	13.67	20.96
F04313–1649	7473.20	-7	(± 3)	125	(± 8)	0.58	($^{+0.07}_{-0.06}$)	0.44	($^{+0.06}_{-0.05}$)	13.41	20.80
F07353+2903	7868.96	-118	(± 3)	319	(± 21)	0.52	($^{+0.07}_{-0.06}$)	0.34	($^{+0.05}_{-0.04}$)	13.77	21.07
F07449+3350:W	8003.32	-9	(± 4)	215	(± 19)	0.29	($^{+0.05}_{-0.04}$)	0.32	($^{+0.06}_{-0.04}$)	13.35	20.64
F07449+3350:E
F08136+3110	8296.23	-63	(± 5)	277	(± 26)	0.22	($^{+0.05}_{-0.02}$)	0.60	($^{+0.14}_{-0.05}$)	13.34	20.64
F08143+3134	8013.52	-400	(± 6)	107	(± 17)	2.00	($^{+1.01}_{-0.46}$)	0.12	($^{+0.06}_{-0.03}$)	13.88	21.18
F08208+3211	8234.34	156	(± 11)	337	(± 56)	0.23	($^{+0.13}_{-0.03}$)	0.41	($^{+0.23}_{-0.05}$)	13.45	20.75
F09567+4119	8021.43	-82	(± 6)	304	(± 30)	0.16	($^{+0.05}_{-0.01}$)	0.99	($^{+0.00}_{-0.00}$)	13.24	20.53
F10156+3705
F10485+3726	7996.15	-13	(± 4)	142	(± 12)	1.28	($^{+0.23}_{-0.18}$)	0.30	($^{+0.05}_{-0.04}$)	13.81	21.11
F16576+3553	8079.64	-219	(± 3)	115	(± 7)	1.22	($^{+0.16}_{-0.12}$)	0.25	($^{+0.03}_{-0.02}$)	13.70	21.00

Note. — Col.(2): Redshifted, heliocentric, vacuum wavelength of the Na I D₁ λ 5896 line; in Å. Col.(3): Velocity relative to systemic, in km s⁻¹. Negative velocities are blueshifted. Components with $\Delta v < -50$ km s⁻¹ are assumed to be outflowing (see Paper II). Col.(4): Doppler parameter, in km s⁻¹. Col.(5): Central optical depth of the Na I D₁ λ 5896 line; the optical depth of the D₂ line is twice this value. Col.(6): Covering fraction of the gas. Col.(7-8): Logarithm of column density of Na I and H, respectively, in cm⁻² (§7).